



**Politecnico
di Torino**

Politecnico di Torino

Corso di Laurea Magistrale in Strumentazione Biomedica

A.A. 2023/2024

Sessione di Laurea: Ottobre 2024

Characterization of a micro-ring resonator based photoacoustic microscopy system

Exploring its potential application in Doppler measurements

Relatori:

Mengyang Liu
Kristen Meiburger
Giulia Rotunno
Ádám Apró

Candidato:

Giorgio Gregnol

SUMMARY

This study investigates the development and optimization of a novel photoacoustic microscopy (PAM) system incorporating a micro-ring resonator (MRR) for advanced ultrasound detection. PAM is a powerful imaging technique recognized for its ability to visualize optical absorption contrast in biological tissues without the need for contrast agents, enabling high-resolution imaging with lateral resolution determined solely by the optical diffraction limit. The primary aim of this research was to construct and refine a device capable of capturing photoacoustic signals generated by a pulsed laser and analyzing these signals to detect the Doppler effect in fluids, potentially facilitating non-invasive measurements of blood flow velocities within complex vascular networks.

Initial tests confirmed the device's capability to generate and detect high-quality photoacoustic images. Key modifications were implemented to enhance the device's performances: a variable neutral density filter was added in the beam path to allow precise control of laser power, a beam block was introduced to absorb excess energy reflected from the filter, and a 3-axis stage was used to couple the excitation beam to an optical fiber, achieving a coupling efficiency of 60%. Additionally, a collimator was introduced to stabilize and direct the laser beam more effectively, and the alignment of the photodetector was optimized to maximize signal-to-noise ratio.

Characterization of the device revealed several critical performance metrics: the Q factor, which indicates the resonator's sensitivity, was found to be lower than expected, potentially due to manufacturing limitations. Nonetheless, the lateral resolution was determined to be 5.5 μm and the axial resolution was measured at 12 μm , offering promising precision for various applications. With a field of view of 0.8 mm, the device proved well-suited for small to medium-sized samples, presenting exciting potential for targeted investigations, though larger specimens may benefit from future enhancements. The device also faced challenges related to signal instability due to waveguide interference, highlighting areas that require further refinement.

Energy stability measurements underscored the importance of optimizing the laser power to maintain consistent signal quality. Despite adjustments, the device did experience some instability due to vibrations caused by a cooling fan of the excitation laser. These vibrations adversely affected the coupling efficiency, resulting in a noticeable loss of energy irrespective of the power setting.

Attempts to detect the Doppler effect in moving microspheres were constrained by the sensitivity of the MRR and the size of the glass cover. These limitations hindered accurate detection of frequency shifts and time delays, indicating that future advancements in MRR design and manufacturing could significantly improve measurement accuracy.

In conclusion, this research advances the field of photoacoustic imaging by optimizing system performances and identifying critical areas for future development. The improvements made and challenges encountered provide valuable insights for enhancing non-invasive vascular research and diagnostic imaging applications, setting the stage for more accurate and versatile PAM systems in the future.

CONTENTS

INTRODUCTION	9
CHAPTER I	11
1 DEVICE	12
1.1 EXCITATION PULSE LASER (PAM SOURCE).....	12
1.2 MIRROR.....	13
1.3 OPTICAL FIBER.....	15
1.4 GALVANOMETRIC MIRRORS	15
1.5 OBJECTIVE	17
1.6 MICRO-RING RESONATOR (MRR)	17
1.7 TUNABLE LASER	19
1.8 PHOTODETECTOR	20
CHAPTER II.....	23
2 DEVICE UPGRADE.....	24
2.1 VARIABLE NEUTRAL DENSITY FILTER	24
2.2 BEAM BLOCK	25
2.3 LASER-OPTICAL FIBER COUPLING	27
2.4 COLLIMATOR	29
2.5 PHOTODETECTOR INPUT.....	30
3 CHARACTERIZATION	34
3.1 Q FACTOR	35
3.2 LATERAL RESOLUTION.....	36
3.3 AXIAL RESOLUTION.....	40
3.4 FIELD OF VIEW.....	42
CHAPTER III	46
4 ENERGY ANALYSIS	47
CHAPTER IV.....	50
5 DOPPLER EFFECT APPLICATION.....	51
6 CONCLUSIONS AND FUTURE DEVELOPMENTS.....	61

7 *BIBLIOGRAPHY*62

INTRODUCTION

INTRODUCTION

Despite the rapid advancements in various optical microscopic imaging technologies, photoacoustic microscopy (PAM) stands out as the sole option for directly visualizing optical absorption contrast in biomedicine without the necessity of contrast agents [1] [2]. When compared to other high-resolution optical imaging modalities such as confocal microscopy, two-photon microscopy, and optical coherence tomography, PAM excels in extracting physiologically specific optical absorption properties in biological tissue, with lateral resolution determined solely by the optical diffraction limit. In PAM, a short-pulsed laser beam is directed onto biological tissues, resulting in a transient thermoelastic expansion that generates ultrasonic waves comprising a wide range of frequency components. These waves can be detected to construct images based on optical absorption contrast. The amplitude of the induced ultrasonic wave is directly proportional to the product of the local optical fluence and the optical absorption coefficient, while the travel time of the wave correlates with the distance between its origin and the ultrasonic detector.

PAM can image both endogenous sources like hemoglobin and melanin, and exogenous contrast agents such as chemical dyes, nanoparticles, and reporter gene products, providing rich anatomical and functional information.

PAM has numerous medical applications. It is widely used for imaging microvasculature, which is valuable in studying tumor pathologies and visualizing angiogenesis. Additionally, it is employed in the imaging of skin tumors, such as melanoma, enabling the detection of melanin distribution and other optical features. PAM can also be used for functional imaging, such as mapping blood oxygenation, and monitoring tissue changes during tumor growth or treatments. However, PAM faces limitations in imaging samples with poor optical absorption. To delve into more complex physiological processes, integrating PAM with established optical microscopic imaging modalities becomes imperative. Despite previous attempts to integrate PAM with confocal microscopy and optical coherence tomography, these efforts have yielded limited lateral and axial resolutions due to constraints in detector design. Optical-based ultrasonic detection techniques offer a promising solution to these challenges.

From a technological standpoint, the most advanced detectors include piezoelectric transducers, optical micro resonators (MRR), fiber-optic interferometers, and capacitive micromachined ultrasonic transducers (CMUT). Piezoelectric transducers are the most common but have limitations in terms of resolution and field of view. Optical micro resonators are miniaturized devices offering high sensitivity and a wide bandwidth (100-150 MHz), improving both resolution and field of view. Fiber-optic interferometers and CMUTs also provide high sensitivity and resolution but can be more complex to integrate.

Among various optical-based ultrasound detection methods, Micro-Ring Resonator (MRR) demonstrates unique advantages [3] [4] [5]. MRR enables highly sensitive ultrasound detection using a sub-millimeter-size device with an ultra-wide frequency response, thereby minimizing interference with the optical path. Additionally, MRR offers a broader ultrasonic detection bandwidth, enhancing saturation limits and axial resolution in functional photoacoustic imaging.

The miniaturized MRR detector allows sensitive ultrasound detection within a larger detection angle, favoring increased field-of-view in laser-scanning PAM systems.

In this study, we designed a device that could record a photoacoustic signal generated by a sample hit with a pulsed excitation laser, and through the signal the device was able to construct a photoacoustic image that could be visualized.

The idea behind this project was to have a device that could detect photoacoustic signals in the best possible way and which, through an analysis of the frequencies contained in them, would be able to detect the Doppler effect (which is a physical phenomenon that describes the apparent change in the frequency or wavelength of a wave in relation to the relative motion between the source of the wave and the observer) of a signal from a fluid (ideally blood) moving at a certain speed.

Once the presence of the Doppler effect has been verified, future studies could demonstrate how, by knowing the angle between the MRR and a tube (ideally a blood vessel) it is easy to trace the speed of the fluid contained in it. Furthermore, by acquiring the signal from different angles it will be possible to develop a device that will be independent of the angle between sensor and tube to be able to exploit this ability to know the speed and direction of blood flow in a complex network of vessels such as that of the human body.

CHAPTER I

1 DEVICE

Before talking about the device built and analyzed in this study on photoacoustic imaging, it is important to analyze its main components and their operation.

1.1 EXCITATION PULSE LASER (PAM SOURCE)

The excitation pulse laser emits short bursts of intense light, effectively stimulating the target tissue to generate acoustic waves. These waves are then detected and translated into detailed images, offering researchers invaluable insights into biological structures and functions at a cellular level. Through precise control and optimization of the excitation pulse laser parameters, such as wavelength and energy, researchers can enhance the imaging resolution and depth.

The used laser was the SOL - COMPACT Q-SWITCHED DPSS LASER at 532 nm produced by Bright Solutions (Fig. 1a), is a green light laser that operates in the fast-switched regime (Q-switched), which means it emits short, high-energy laser pulses, making it particularly suitable for applications requiring precision and power. The power and frequency of these pulses can simply be changed through a digital control box (Fig. 1b).

Furthermore, the designation "DPSS" stands for "diode-pumped solid-state", which means that this laser is pumped by laser diodes rather than plasma lamps as in older lasers. This allows for greater efficiency.



a.



b.

Figure 1 | Excitation laser main components. (a) Laser's box with air cooling fan. (b) Digital control box for simplified remote control which allows to turn the laser on/off, modulate the frequency (from 1kHz to 80kHz) and modulate the power (from 0% to 100%).

1.2 MIRROR

The mirrors tailored for laser applications enable precise control and manipulation of light paths to optimize imaging quality. These specialized mirrors are engineered to exhibit high reflectivity across specific wavelengths of interest, ensuring efficient redirection of laser beams. Furthermore, advanced mirror coatings minimize undesired scattering and absorption, preserving the integrity of the laser pulses and maximizing signal strength for robust photoacoustic signal acquisition.

The mirrors were mounted on special supports (Fig. 2a) and adequately fixed to the workstation via posts, pedestal post holders and clamping forks (Fig. 2b). In this way, once the beam was properly calibrated, we had a stable system (Fig. 2c).



a.



b.



c.

Figure 2 | Main components for fixing the mirrors. (a) Mirror support with screws to adjust the direction of the beam in two dimensions. (b) From left to right we have post, pedestal post holder and clamping fork. (c) Final setup.

1.3 OPTICAL FIBER

The optical fibers serve as essential components for delivering laser light to the target sample and collecting the generated acoustic signals for imaging purposes. Optical fibers used in PAM systems (Fig. 3) are designed to efficiently transmit laser light of specific wavelengths to the sample. Once the laser light interacts with the target tissue, it induces localized heating, leading to the generation of acoustic waves due to thermal expansion. These acoustic waves contain valuable information about the tissue's structure and properties. Optical fibers are employed to capture and guide these acoustic signals to the detection system for further processing and image reconstruction.

We decided to use a single-mode optical fiber has a small core (about 8-10 micrometers) that allows only one light mode to travel, reducing modal dispersion and maintaining signal integrity over long distances. This ensures high beam quality and minimal signal distortion, making it ideal for precise applications like Photoacoustic Microscopy (PAM), where coherent laser pulses are crucial for high-resolution imaging of biological tissues. Single-mode fibers enhance the clarity and accuracy of photoacoustic signals, improving imaging performances.



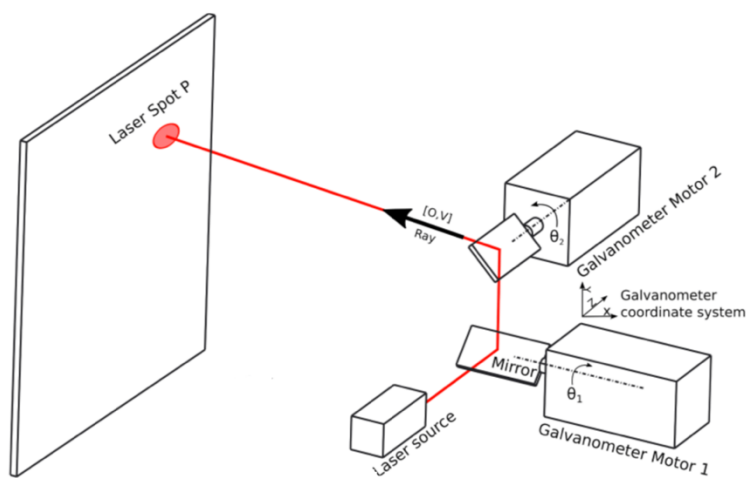
Figure 3 | *Used single-mode optical fiber.*

1.4 GALVANOMETRIC MIRRORS

Galvanometric mirrors are critical components in various optical systems, particularly laser scanning applications. These mirrors are typically small, lightweight, and highly reflective, often made of materials like silicon or gold-coated glass. Their functionality relies on the principle of electromechanical deflection.

Essentially, galvanometric mirrors work by leveraging the interaction between an applied electrical current and a magnetic field to control the position of the mirror. The mirror is mounted on a torsion beam within a magnetic field generated by a coil or permanent magnet. When an electrical current passes through the coil, it creates a magnetic field that interacts with the mirror's magnetic moment, causing it to rotate (Fig. 4a). This rotation enables precise control over the direction of the reflected laser beam. By modulating the current applied to the coil, the angle of deflection of the mirror can be finely adjusted (Fig. 4b).

Overall, galvanometric mirrors play a crucial role in enabling precise and dynamic control of laser beams, making them indispensable in a wide range of scientific applications, in our case they allowed us to move the beam on the sample during the imaging phase, to be able to scan a square portion.



a.



b.

Figure 4 | Geometry and working principle of the galvanometric mirrors. (a) Working principle of the galvanometric mirrors. (b) Used galvanometric mirrors.

1.5 OBJECTIVE

The objectives (Fig. 5), in photoacoustic technology, are used to optimize the resolution and sensitivity of images acquired by laser beams. They are exploited to maximize the collection of photoacoustic signals generated by the interaction between the laser beam and the sample of interest. These optical components are designed to focus the laser beam efficiently on the sample, ensuring uniform energy distribution and maximizing the depth of penetration into the material. Additionally, objectives can be designed to allow focusing on different depths in the sample, allowing for detailed three-dimensional visualization. We used the Olympus UPlanSApo 4x/0.16na Objective with a working distance of 13 mm, this means that the sample had to have this distance from the exit of the objective to focus the beam on it as much as possible.



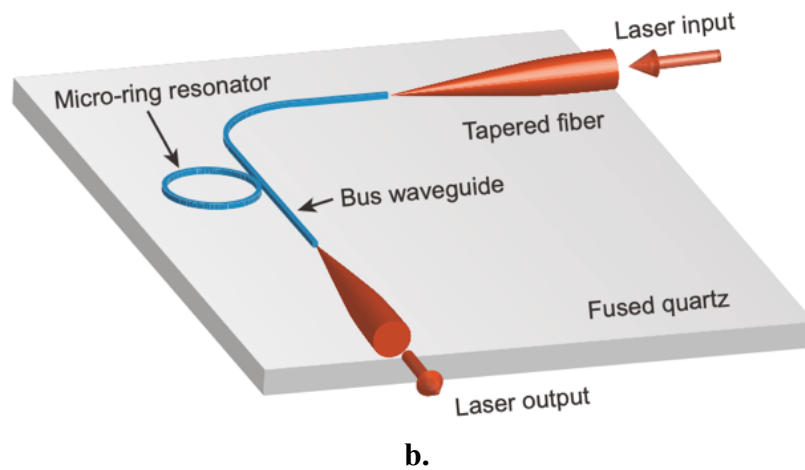
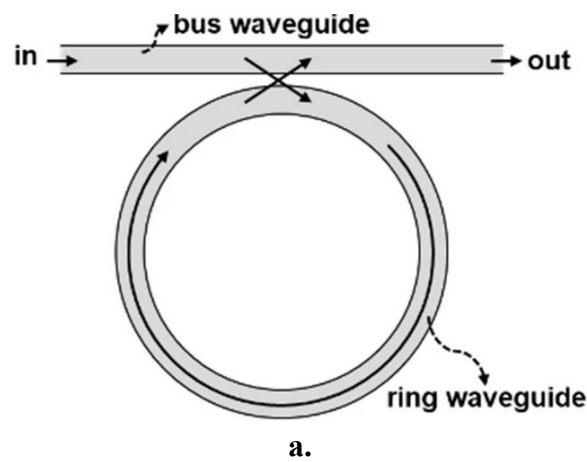
Figure 5 | *Used objective.*

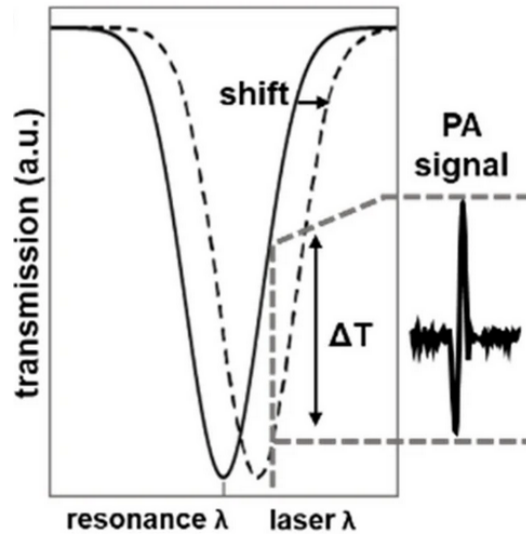
1.6 MICRO-RING RESONATOR (MRR)

Micro-ring resonators (MRRs) have proven to be highly effective in photoacoustic imaging, delivering exceptional sensitivity and resolution for biomedical uses. Fabricated from optical materials like silicon using advanced techniques such as photolithography and etching, MRRs possess dimensions on the order of micrometers, they are made up of a bus waveguide and a ring waveguide (Fig. 6a), finely tuned to resonate with incoming light waves (Fig. 6b). When a photoacoustic signal, generated by the interaction of light and matter, strikes the MRR, it induces

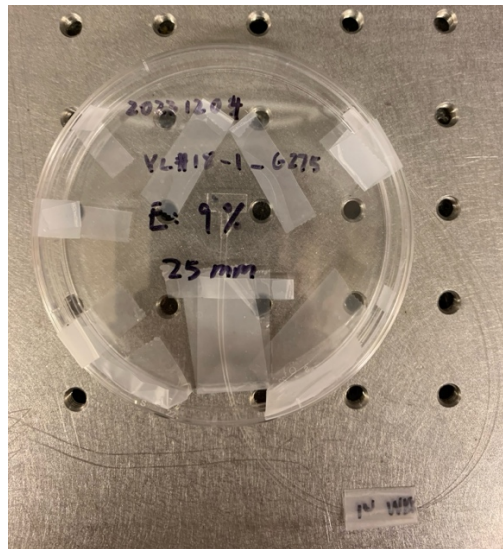
vibrations in the material of the micro resonator. These vibrations alter the refractive index of the material, causing changes in the resonant frequency of the device. As a result, the transmission spectrum of the micro resonator exhibits oscillations that can be analyzed to determine the presence and characteristics of the photoacoustic signal. Thus, variations in light transmission through the MRR provide information about the original signal, enabling highly sensitive and precise detection (Fig. 6c).

The MRR we used in this project was provided to us by Northwestern University thanks to collaboration between departments (Fig. 6d).





c.



d.

Figure 6 | Geometry and working principle of the MRR ultrasonic detector. (a) Geometry of the MRR [6]. (b) MRR integrated with a tunable laser and two optical fibers [6]. (c) Transmission spectrum of an MRR (measured with a DC photodetector) with the PA signal detected (the solid line represents the transmission spectrum in the absence of ultrasound and the dotted line represents an oscillation of the transmission spectrum in the presence of ultrasound) [6]. (d) Used MRR with the optical fiber coupled.

1.7 TUNABLE LASER

Tunable lasers, when paired with resonant micro rings, are essential in photoacoustic imaging because they allow for precise control over light generation and manipulation. This precise

control is crucial for optimizing wavelength tuning, which is key to achieving maximum sensitivity and resolution in photoacoustic images, reaching the wavelength found at the steepest point of the left wall of the MRR resonance peak. We used the Manual Tunable Littman/Metcalf Diode Laser System from Lion company at 780 nm. By finely adjusting the wavelength, these lasers can be tailored to match the optical properties of the sample being examined, resulting in clearer and higher-quality images (Fig. 7). This precise tuning also helps in identifying the specific absorption characteristics of biological tissues, making it easier to distinguish different structures and see fine details. Additionally, using tunable lasers with resonant micro rings provides flexibility in experiments, allowing imaging settings to be quickly adjusted to suit various experimental conditions.



Figure 7 | Used tunable laser and its controller.

1.8 PHOTODETECTOR

Photodetectors are essential in optical applications for converting light signals into electrical signals that can be measured. In our project, we used two different photodetectors (one for measuring the resonance spectrum and the other for measuring the photoacoustic signal).

For the spectrum we used DET36A/M - Si Detector, 350 - 1100 nm (Fig. 8a) and for the signal we have chosen the MENLO SYSTEMS APD210 photodetector (Fig. 8b). The APD210, which uses avalanche photodiode (APD) technology, provides exceptional sensitivity and quick response times, allowing for the accurate and prompt detection of faint optical signals. This high sensitivity enables the APD210 to detect very low levels of light, making it ideal for applications where the optical signal is weak. Additionally, the rapid response time of APD technology ensures fast detection and processing of light signals, which is critical for high-speed data acquisition applications.



Figure 8 | Used photodetectors. (a) Used DC photodetector.
(b) Used AC photodetector.

The starting device we assembled was based on an excitation laser (PAM source), with the task of hitting the target (via a series of mirrors, two galvanometric mirrors and an objective x4) and generating the photoacoustic wave. The signal was transmitted to a photodetector via an optical fiber, amplified, and sent to a PC for processing (Fig. 9).

For our experiments, both the target and the MRR were immersed in a water tank to prevent the photoacoustic waves from dissipating into the air.

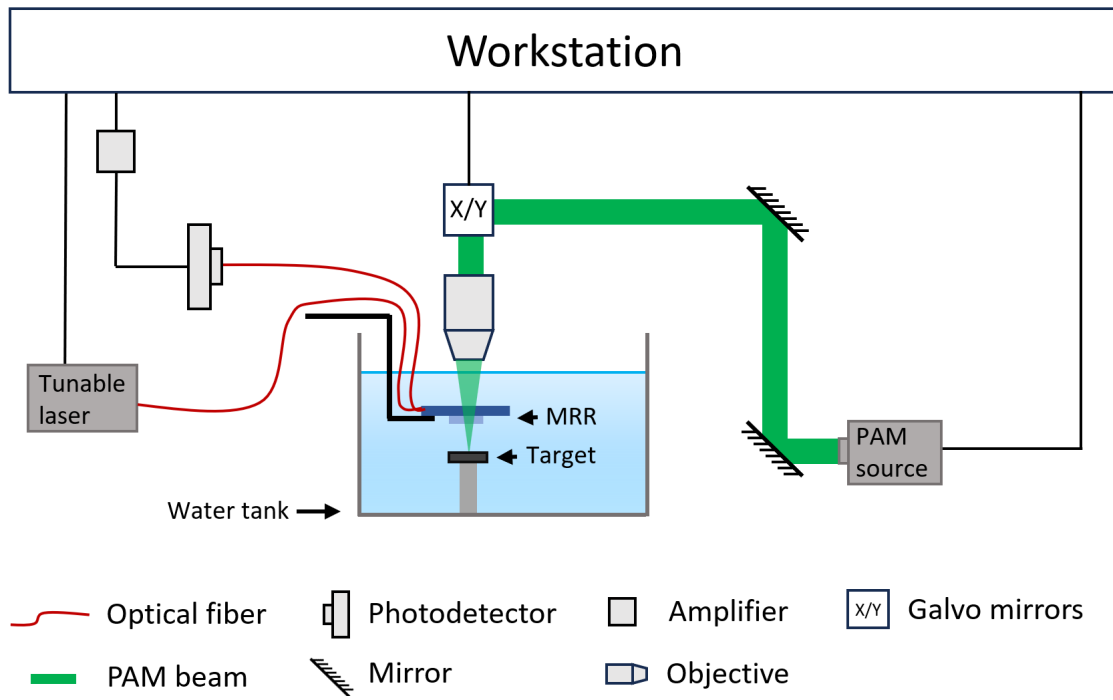


Figure 9 | Schematic of the starting device.

CHAPTER II

2 DEVICE UPGRADE

The initial device had been previously tested to ensure it could acquire a photoacoustic signal from a simple sample and reconstruct a photoacoustic image using the recorded data. While the performances were not optimal, the device showed promising potential for future improvements and developments.

We first decided to make some minor adjustments to the initial setup to minimize laser beam loss and enhance the system's resolution during imaging. The methods used to calculate the performances will be discussed later.

2.1 VARIABLE NEUTRAL DENSITY FILTER

The first modification made was to insert a variable neutral density filter (Fig. 10a) immediately after the exit of the excitation laser, to be able to change and control the power of the beam without acting on the laser settings every time but making this operation much easier and faster.

Furthermore, we also made this choice to ensure that we do not damage the optical fiber (which will be discussed in section 2.3) with too high power (an event that occurred during the coupling of the laser with the optical fiber). The filter was mounted and fixed to the workstation via post, pedestal post holder and clamping fork (Fig. 10b). As we can see from the images, just change the point of incidence of the beam on the filter by simply turning the wheel to obtain a different attenuation (0° corresponds to 0% attenuation and 360° corresponds to 100% attenuation).



a.



b.

Figure 10 | Components and assembly for beam attenuation.
(a) Used variable neutral density filter. (b) Final setup.

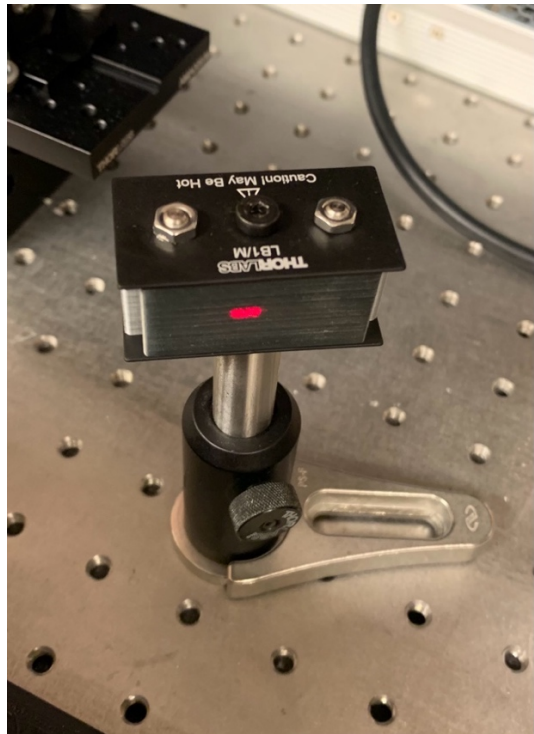
2.2 BEAM BLOCK

After inserting the density filter was useful to use a beam block (Fig. 11a) to improve the safety of the device because the beam that was not transmitted was reflected elsewhere and could result dangerous. The beam block used had the task of blocking and absorbing laser beams with wavelengths between 400 nm and 2 μm and with an average maximum power of 10 W, both for continuous wave lasers and pulsed lasers as in our case. It has proven useful for preventing unwanted reflections and dispersions, protecting delicate instruments and ensuring operator safety from potentially dangerous laser radiation.

It was fixed to the workstation via post, pedestal post holder and clamping fork as shown in the figure below (Fig. 11b).



a.



b.

Figure 11 | Components and assembly for beam block.
(a) Used beam block. (b) Final setup.

2.3 LASER-OPTICAL FIBER COUPLING

The first change we did was coupling an optical fiber and the laser beam coming out of the series of mirrors. We placed a narrow FC/PC connectorized fiber holder (Fig. 12b) on top of a 3-axis nano stage (Fig. 12a), which is an advanced device designed for precise three-dimensional movement control (X, Y, and Z) on a nanometric scale. This setup allowed for accurate positioning of the optical fiber, ensuring it was aligned parallel to the laser beam. Additionally, the fiber holder could be securely fastened with screws, providing excellent stability during operation.

After that we fixed on the side of the nano stage a mounting bracket (Fig. 12c), and on the top of it a lens holder (Fig. 12d), using an adapter we mounted a convex lens (Fig. 12e) with a focal distance of 13.9 mm for focalizing the beam inside the core of the optical fiber. These two latter components remain fixed and only the fiber holder moves through the nano-stage knobs.

After assembling the various components (Fig. 12f), we had to make sure to optimize the efficiency of the coupling. This was done following the steps below:

- Setting the excitation laser power to 100 μW and the frequency to 1 kHz (to make sure not to damage the optical fiber with too high power and to facilitate the calculation of efficiency).
- Aligning the mirrors, turning the screws on them, ensuring that the beam enters perfectly into the center of the lens for the focalization of the beam.
- Connecting a multi-mode optical fiber to the fiber holder (because it has a bigger core compared to the single-mode optical fiber and is therefore easier to align).
- Connecting the other end of the optical fiber to a power meter.
- Turning the knobs of the three axes of the nano stage trying to reach the highest power changing the position of the optical fiber.
- Changing the multi-mode optical fiber with the single-mode optical fiber (since by now the beam should be in a good position and therefore easier to align with a smaller core).
- Turning again the knobs of the three axes of the nano stage trying to reach the highest power.

Once this procedure was carried out with maximum precision the power meter measured 60 μW we therefore ascertained that the coupling efficiency was 60%.



a.



b.



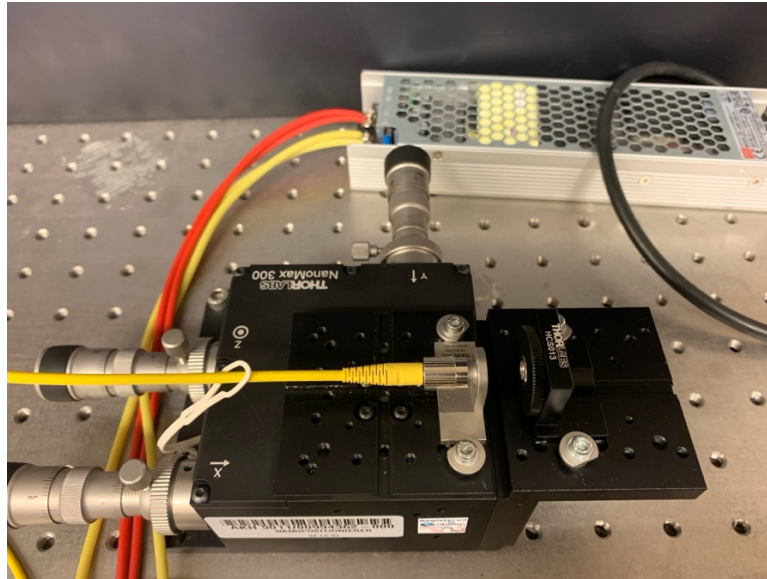
c.



d.



e.

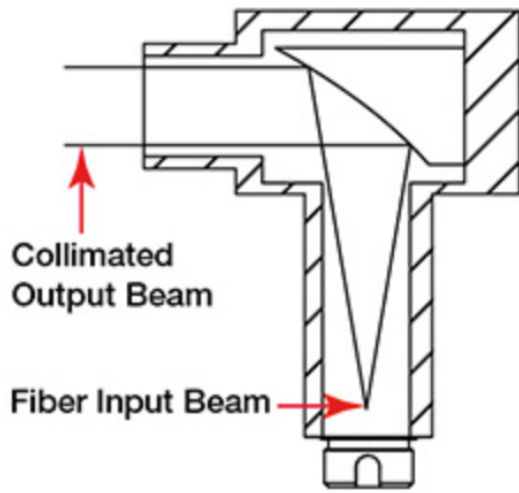


f.

Figure 12 | Components and assembly for laser-optical fiber coupling. (a) Used 3-axis nano stage. (b) Used narrow key FC/PC-connectorized-fiber holder. (c) Used mounting bracket. (d) Used lens holder. (e) Used lens. (f) Final setup.

2.4 COLLIMATOR

Once the laser and the optical fiber were coupled, we needed to direct and stabilize the beam towards the galvo mirrors, and we did this using a protected silver reflective collimator. A protected silver reflective collimator operates by using reflection and optical focusing. Light, originating from a laser source or an optical fiber, enters the collimator through an FC/PC connector. Inside, a parabolic mirror coated with silver reflects the light (Fig. 13a). Silver, chosen for its high reflectivity, is protected by a layer that prevents oxidation and degradation. The curved surface of the mirror focuses the light to a specific point, creating a parallel beam. This ensures a highly parallel and focused beam. We therefore connected the optical fiber to the collimator (Fig. 13b) and fixed the collimator to a mirror mount (Fig. 13c) which allowed us to adjust the direction of the beam in two directions (vertical and horizontal), to direct the beam perfectly in the middle of the first galvo mirror to reduce beam loss. In the end we fixed everything to the workstation via post, pedestal post holder and clamping fork (Fig. 13d).



a.



b.



c.



d.

Figure 13 | Components and assembly for beam collimation. (a) Operating principle of the collimator. (b) Used protected silver reflective collimator. (c) Used mirror mount. (d) Final setup.

2.5 PHOTODETECTOR INPUT

Doing preliminary measurements on the efficiency of the optical fibers we noticed that the space between the input of the photodetector (i.e. where the light sensor is located) and the output of

the optical fiber coming out of the MRR was too wide. The cause of this was the adapter used to connect the optical fiber to the photodetector. So, to improve efficiency (and therefore to have a wider signal), we decided to remove the adapter from the photodetector, break and clean the optical fiber and insert it onto a 3-axis nano stage via a fiber chuck mount (Fig. 14a) and a fiber chuck (Fig. 14b).

The final setup (Fig. 14c) allowed us to maximize the signal recording efficiency thanks to:

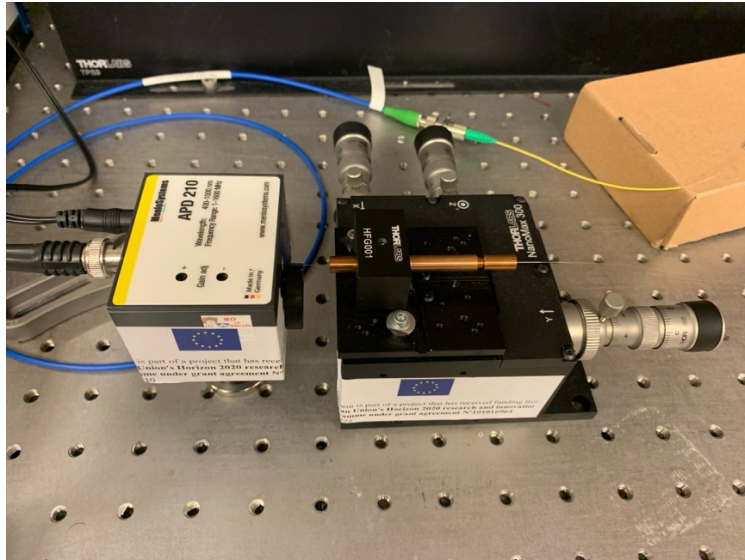
- The Impact with the beam perpendicularly on the sensor, to maximize light absorption and minimize its reflection.
- The output of the optical fiber brought as close as possible and very precisely to the sensor moving the stage knobs.



a.



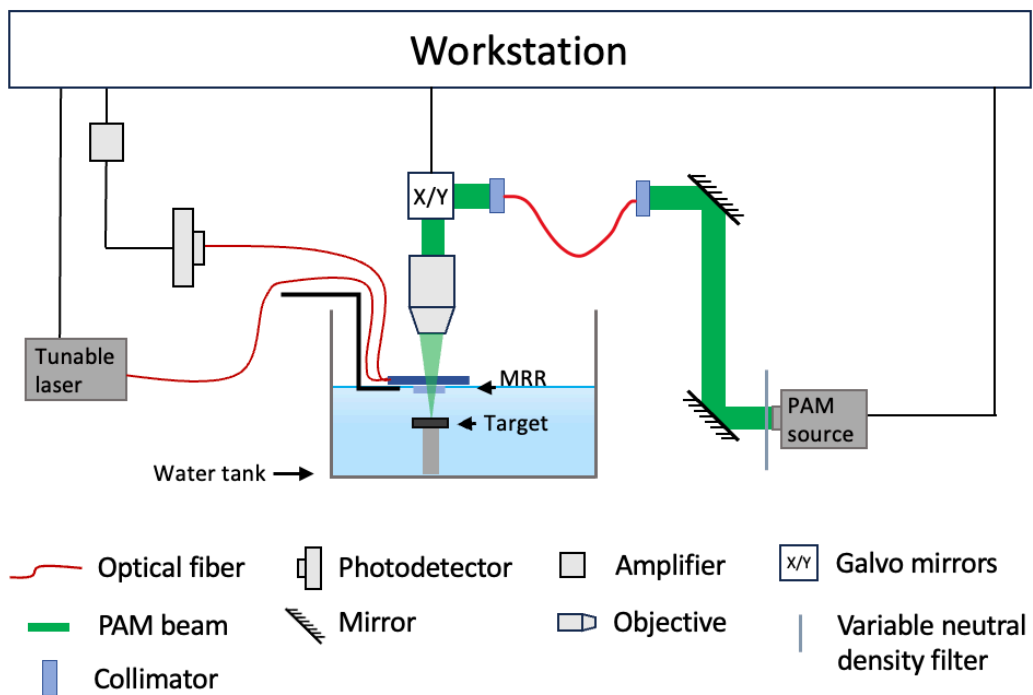
b.



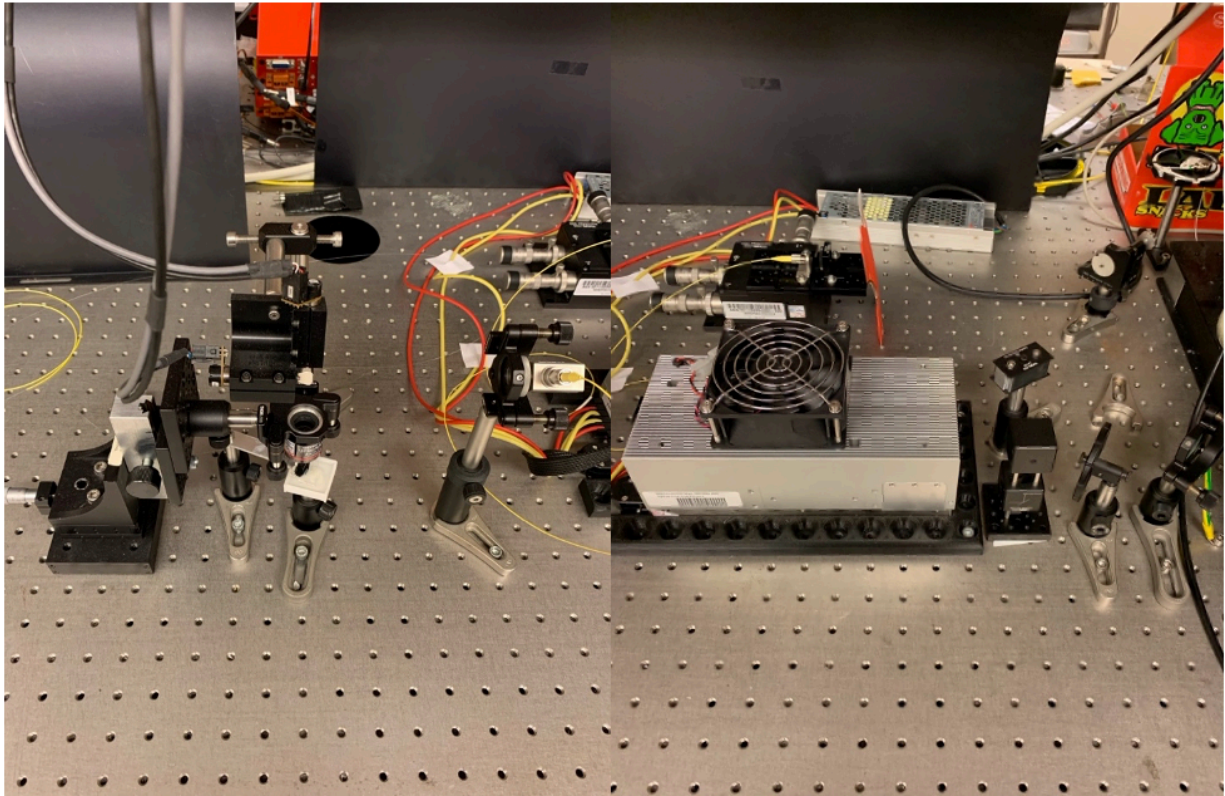
c.

Figure 14 | Components and assembly for the photodetector setup. (a) Used fiber chuck mount. (b) Used fiber chuck. (c) Final setup.

After the modifications listed above, and after aligning the beam making sure to have the maximum possible power on the sample, the final device looked like the one shown in the figure below (Fig. 15a, Fig. 15b).



a.



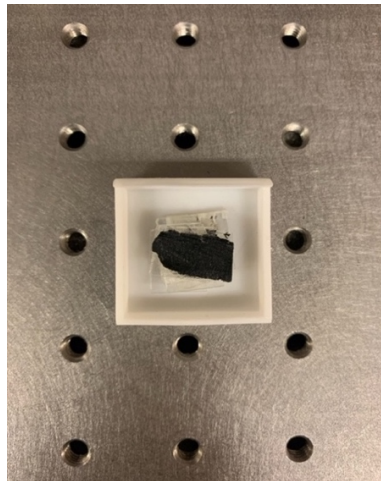
b.

Figure 15 | *Final setup.* (a) *Schematic of the final setup.*
(b) *Photo of the device.*

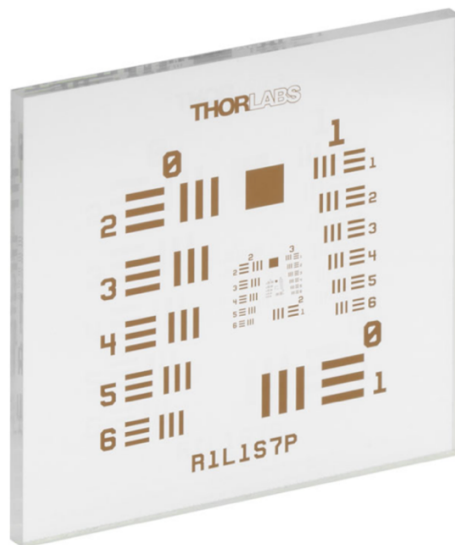
3 CHARACTERIZATION

Once we prepared the device for use, we decided to analyze its performances. We initially used a black tape as a sample (Fig. 16a) which allowed us to find the photoacoustic signal easily by modifying the position of the objective to set the focal point on the sample based on the distance at which we had positioned it from the MRR. Then moving on to an USAF sample from Thorlabs (Fig. 16b) with parallel lines and well-defined edges to be able to extract all the necessary parameters to analyze the performances.

The sensor utilized was an array of MRRs rather than a single MRR; however, only the middle one was operational. This design choice was intentional, as the university that developed the array had future advancements planned for MRR arrays.



a.



b.

Figure 16 | Samples. (a) Used black tape.
(b) Used USAF sample.

In a PAM (Photoacoustic Microscopy) device, key performance metrics include the Q factor, axial resolution, lateral resolution, and field of view. The Q factor, or quality factor, indicates the efficiency of the optical resonator in confining light, influencing the signal-to-noise ratio and overall sensitivity of the imaging system. Axial resolution refers to the ability to distinguish two points along the optical axis; higher axial resolution allows for better depth discrimination in tissue imaging. Lateral resolution, on the other hand, measures the system's capacity to differentiate points in the plane perpendicular to the optical axis, crucial for achieving detailed images of structures. Finally, the field of view defines the extent of the area that can be imaged at once, impacting the overall coverage and speed of imaging in each sample. Together, these parameters determine the imaging quality and capability of PAM devices in biological applications.

3.1 Q FACTOR

The first step was to record the resonance spectrum of the MRR to understand where to set the wavelength of the tunable laser. Once acquired, the Q factor of the MRR could easily be calculated as the first parameter for the characterization of the device.

The Q factor was calculated by [6]:

- Acquiring the spectrum.
- Performing the Lorentzian fit.
- Looking for the peak to peak.
- Dividing it by two.
- Searching for the points on the curve that correspond to these values.
- Finding the distance between the two identified points on the curve ($\Delta\lambda$ = width of the resonance curve at half the maximum amplitude).
- Finding the minimum of the curve (λ_0 = central wavelength of the peak).
- Dividing the minimum by the previously calculated distance ($Q = \lambda_0 / \Delta\lambda$).

These steps led us to obtain a Q factor of 4.47×10^4 as shown in the figure below (Fig. 17).

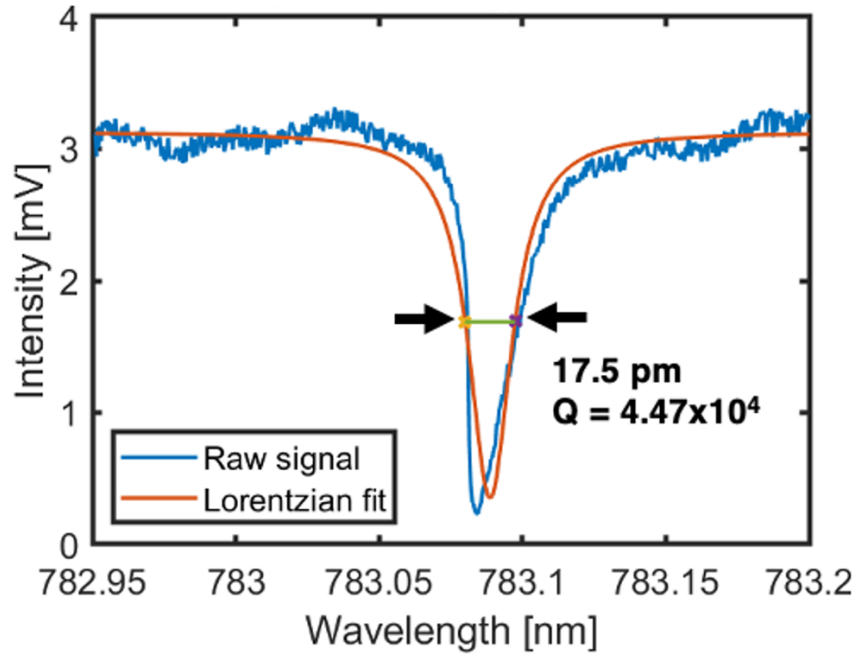


Figure 17 | Resonance Spectrum and Q factor evaluation.

A high Q factor can improve the sensitivity of the device because a high Q factor indicates that the device can operate with a narrow bandwidth, reducing noise and improving the quality of the modulated signal.

Comparing this result with what was reported in the literature, we had a somewhat low Q factor (3x less than NWU's published one [7]), but there was nothing we could do to increase it as it is a parameter that depends on the manufacturing.

3.2 LATERAL RESOLUTION

Before explaining the following step is important to understand how data acquisition worked.

The fundamental principle underlying the system is the synchronization between the excitation laser and the data acquisition card. A trigger signal with a 1 ns pulse width and a frequency of 20 Hz was used, resulting in a laser excitation pulse every 50 ms ($T = 1 / f$) (Fig. 18). The software was configured with a sampling frequency of 1 GHz and 4096 samples, allowing the laser to fire a pulse simultaneously with the acquisition of the 4096-sample signal upon receiving a trigger. Each acquisition lasted approximately 4.096 μ s, calculated by the formula (time = number of samples / sampling frequency).

The second step was to record the photoacoustic signal using the black tape, and once we found it, we replaced the tape with the USAF sample at the same distance (Fig. 19) to acquire an image suitable for calculating the lateral resolution of the device.

To build an image starting from the simple photoacoustic signal, the process that the software followed was to calculate the peak to peak of an epoch (4.096 μs long), average it to have more precise and reliable values with the peak to peak of the x epochs that we decided a priori (ex: if number of averages (NoA) = 3, averages the peak to peak of three successive epochs), and starting from the image pixel at the bottom left he inserted the value obtained proceeding along the entire line to the right and then continuing with the next line (always starting from the left) as shown in the figure below (Fig. 20).

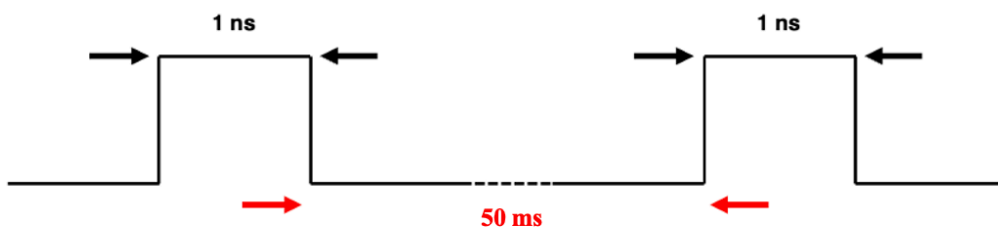


Figure 18 | *Trigger signal diagram.*

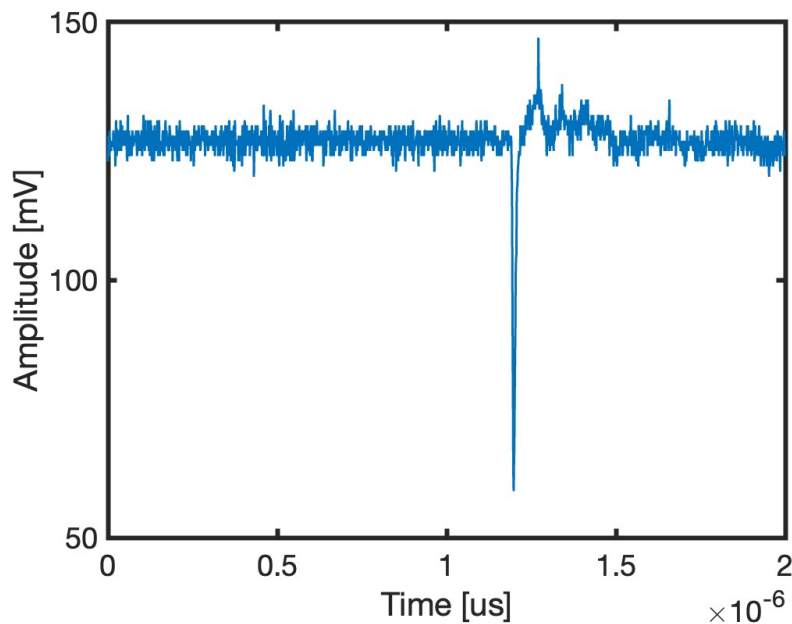


Figure 19 | *USAF sample 2 μs cut epoch of a photoacoustic signal.*

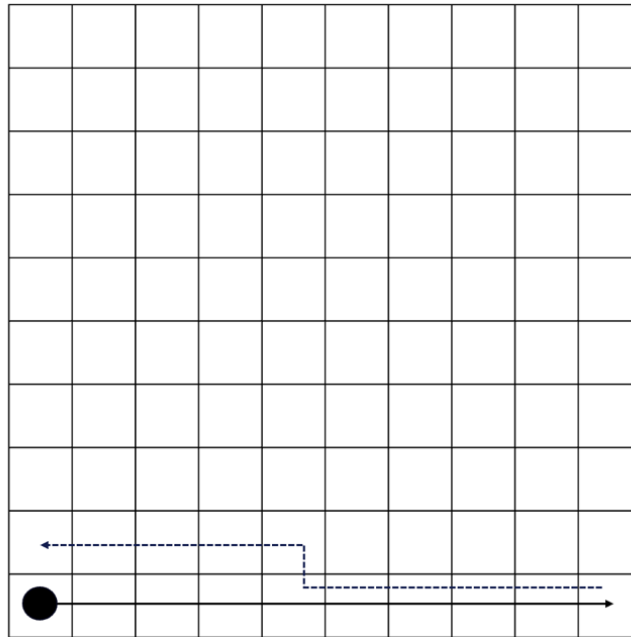


Figure 20 | *Scheme that the software follows to create the image.*

The distance between the sample and the MRR is easily calculable from this graph through a few simple steps: Knowing that the speed of sound in water at room temperature is approximately 1500 m/s, through the law of average speed (velocity = space / time) taking as time the time where we detect the photoacoustic signal is easy to understand that the distance is 1.8 mm ($s = 1500 \text{ m/s} \cdot 1.2 \times 10^{-6} \text{ s}$).

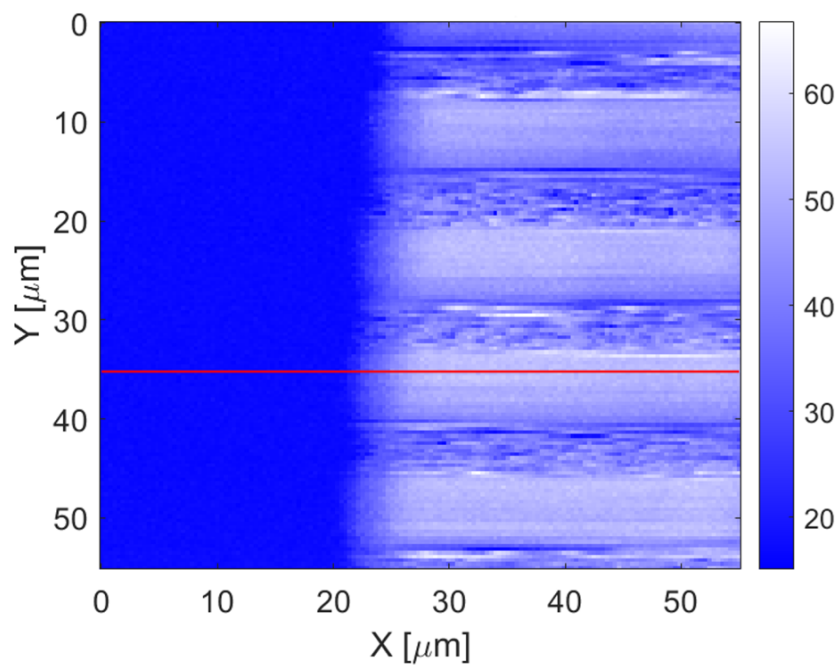
Once these small steps were followed, the goal was to calculate the lateral resolution of the system which describes the minimum distance between two points along a direction perpendicular to the direction of propagation of the wave or light, which can be correctly distinguished as two separate points rather than one single point or a single indistinct structure. To do this we needed to acquire an image as small as possible and as sharp as possible of the edge of a line, and we also needed to know how big an image we were acquiring.

To understand the size of the image we were acquiring, we set the size of the image at 110 x 110 pixels and we acquired an image of the USAF sample, which allowed us, by consulting the website of the company that produces it and reading the size of the analyzed line, to know how big that image was to then be able to zoom and through a scale factor to know the dimensions of our final image.

The best image we were able to capture is shown below (Fig. 21a) with a dimension of 55 μm x 55 μm (always maintaining the same number of samples set previously), NoA of 10 and an energy of the excitation laser on the sample of 75 nJ (with an excitation laser power set by the controller of 50%). The choice of power was made by doing various tests trying to find a good size of the signal (it had to be as large as possible to allow us to have a good image) and avoiding overheating the sample with too high power which would damage it burning its lines.

These steps were followed to calculate the lateral resolution [6]:

- Select a sharp line in the image.
- Plot the distribution of the values of the selected line (placing the distance and not the samples on the x-axis).
- Perform polynomial interpolation of row data (extracting the fitting curve).
- Evaluate the derivative of the fitting curve.
- Look for the peak to peak of the derivative.
- Divide it by two.
- Look for where the derivative curve takes on that value.
- Calculate the distance (in μm) between the two values found (lateral resolution = distance) (Fig. 21b).



a.

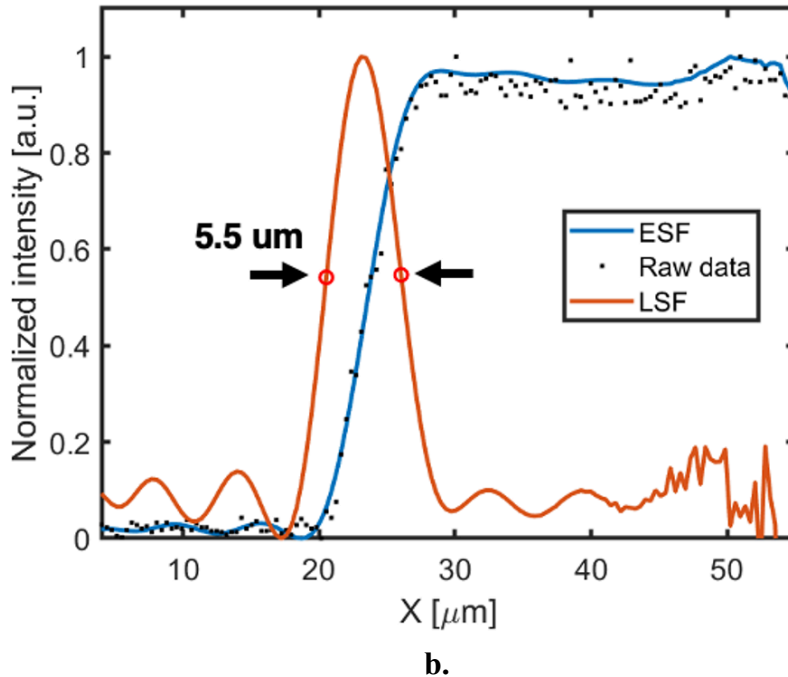


Figure 21 | Lateral resolution evaluation. (a) Image captured $55 \mu\text{m} \times 55 \mu\text{m}$ with the selected line highlighted in red (the color bar represents the values acquired by the data acquisition card with 8 bits). (b) Graph showing the distribution of raw data, the fitting curve in blue and the derivative in red. The two highlighted points represent the half of the peak to peak.

Once these steps have been followed, we have extracted a lateral resolution of $5.5 \mu\text{m}$ from the final graph.

Unfortunately, as can be seen from the image (Fig. 21a), the analyzed line does not seem to have a well-defined profile, in fact some lines of the image are blurred and lose quality (for example from $28 \mu\text{m}$ to $34 \mu\text{m}$). We therefore decided to observe the signal for a long period of time, and we noticed that the problem was the instability of the excitation laser, that is, after a few seconds we could see a random decrease in the signal which then returned to its initial state. Unfortunately, the cause of this event is still unknown to us, but we'll talk about that later in section 4.

3.3 AXIAL RESOLUTION

The third step was to evaluate the axial resolution which is a measure of the system's ability to distinguish between two points located along the axis of propagation of the ultrasonic signal. It is a feature used for determining the quality and precision of the images obtained.

To calculate it we used the same image evaluated previously since we only needed an epoch with a good signal and work on it.

These steps were followed to calculate the axial resolution [6]:

- Select a nice epoch where the signal was present.
- Cut the epoch by analyzing only the part where the signal was.
- Find the absolute value of the signal (ABS).
- Look for the peak to peak of the ABS.
- Divide it by two.
- Look for where the ABS curve takes on that value.
- Calculate the distance (in ns) between the two values found (Fig. 22).
- Multiply the value found with the speed of the ultrasound in the water and thus find the axial resolution ($s = v * t$, $s = 1500 \text{ m/s} \cdot 8 \times 10^{-9} \text{ s}$).

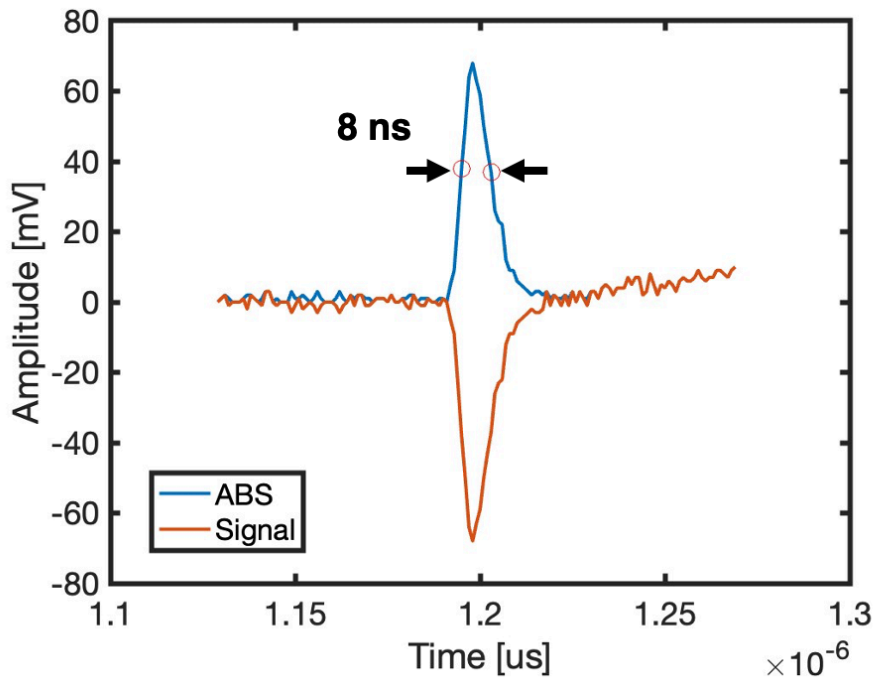


Figure 22 | Axial resolution evaluation.

Once these steps have been followed, we have extracted an axial resolution of $12 \mu\text{m}$ from the final graph and is a good result according to the literature [8].

3.4 FIELD OF VIEW

The fourth step was to evaluate the field of view (FOV), or the size of the area or volume that can be captured in an image. To do this, however, we needed a different image from the one acquired previously, because now the focus was no longer the smallest possible area of the sample, but the largest possible area of the sample. Then we acquired a second image using the black tape with a size of 1.1 mm x 1.1 mm, 110 samples on both the vertical and horizontal axis, NoA of 10 and an energy of the excitation laser on the sample of 75 nJ (Fig. 23).

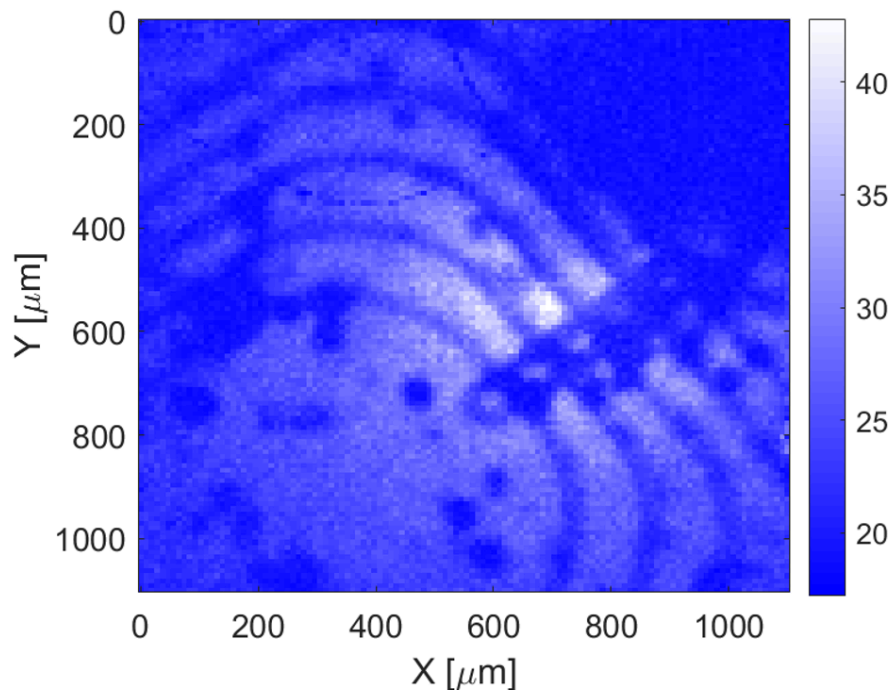


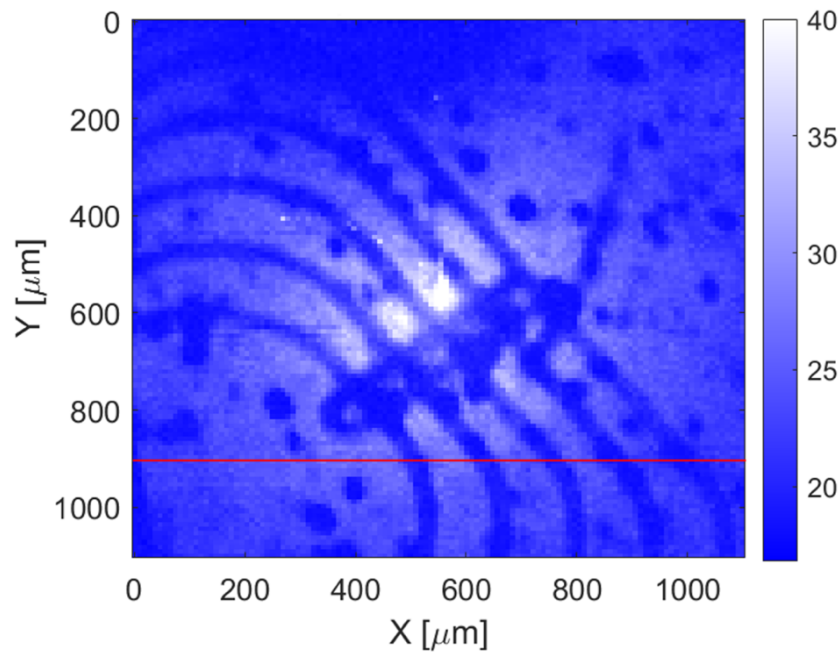
Figure 23 | *Black tape image 1.1 mm x 1.1 mm.*

From as we can see in the image above, however, we notice a large interference due to the MRR, as all the bus waveguides and ring waveguides of the sensor can be seen (The sensor utilized was an array of MRRs, but only the middle one worked, as previously mentioned). We still don't know exactly what caused this phenomenon, and not even the Northwestern University has been able to give us an explanation. This caused some small problems when calculating the field of view which we will talk about later. There were also small bubbles in the image due to dust and other debris present on the MRR interface due to manufacturing, so it was impossible for us to remove them.

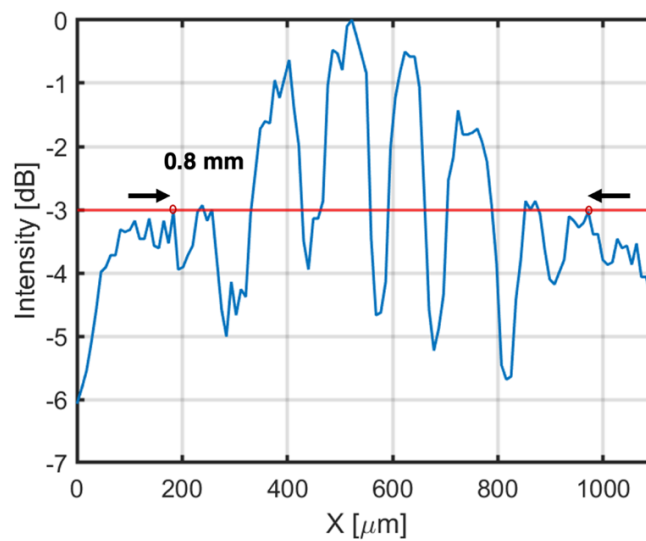
Once the previous image was acquired, we acquired another image using the USAF sample (Fig. 24a) and maintaining the same parameters set previously, to proceed with the calculation of the field of view, because, as in the previous steps, the irregular surface of the black tape is not optimal for this evaluation.

These steps were followed to calculate the lateral resolution:

- Select a sharp line in the image, trying to avoid the waveguides of the MRR.
- Plot the distribution of the values of the selected line (placing the distance and not the samples on the x-axis).
- Find the maximum value of the signal.
- Decrease it by 3dB (-3dB).
- Look for where the curve takes on that value.
- Calculate the distance (in mm) between the two values found (field of view = distance) (Fig. 24b).



a.



b.

Figure 24 | Field of view evaluation. (a) USAF sample image with the analyzed line highlighted. (b) Graph showing the distribution of raw data and the two highlighted points represent the intersection with the value at -3dB.

As we can see from the graphs above, we notice some signal drops due to the presence of the waveguides in the image, this therefore made it more difficult to decide which intersection points between the curve and the -3dB value to select. Our decision was in the end to select the first and last points as intersections, implying that the falls in the middle were not a defect of the device but only the presence of the waveguides.

By doing so, the field of view of the device was found to be 0.8 mm, which in accordance with the needs of biologists, i.e. a field of vision three times larger but unfortunately still unrealized, still turned out to be a somewhat low value.

Due to the visibility issues encountered with the waveguides, we decided to capture additional images using the USAF sample at various distances from the MRR, maintaining the same settings as previously used (Fig. 25). Our goal was to determine if this distance could influence the observed phenomenon.

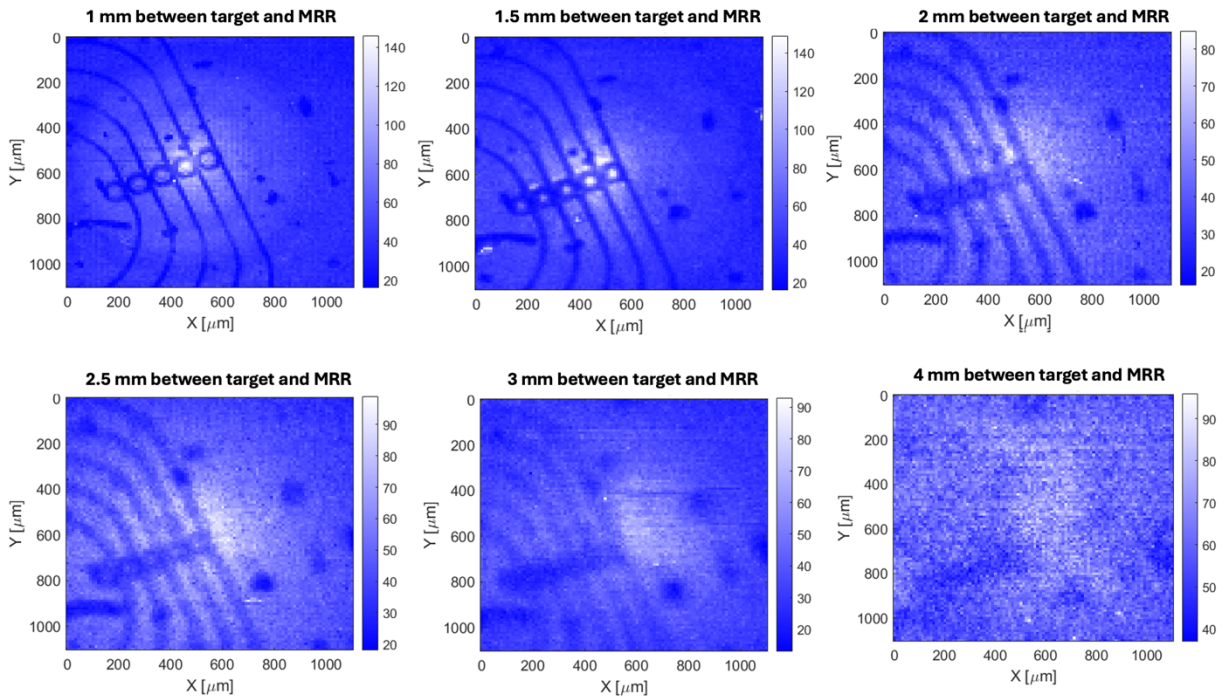


Figure 25 | Images of the USAF sample at different distances from the MRR 1.1 mm x 1.1 mm.

As shown in the figure, interference from the waveguides was noticeable at shorter distances and diminished at greater distances. However, at these larger distances, the signal was no longer uniform, and the noise level was too high. We hypothesized that the excitation laser beam was obstructed by the waveguides, preventing it from reaching the underlying sample and thereby

inhibiting the generation of the photoacoustic signal. The farther the sample was from the MRR, the smaller the shadow area created, and vice versa.

Summarizing, the device we built had good performances to analyze small-medium sized objects (thanks to a high lateral resolution) and slightly less good performances if it was necessary to analyze large samples (due to a field of view that wasn't very high).

CHAPTER III

4 ENERGY ANALYSIS

Due to the excitation laser instability problems encountered during the characterization of the device, especially during the analysis of the lateral resolution, we decided to carry out measurements with an energy meter at the laser output to verify its stability. In this way the goal was to understand what % of laser power should be set in its controller to maintain a stable beam over time.

The measurements were made with the sensor after the variable neutral density filter, to be able to set the energy around 100 nJ (using a pulse frequency of 1 kHz and a power of 100 μ W) and then observe the oscillation of the recorded signal. We started from a power of 10% moving in steps of 10 until we reached 40%, and then continued in steps of 5 until we reached 95%, always analyzing epochs of approximately 60 s.

Once the signals were recorded, we calculated their standard deviation (Fig. 26), because it is a statistical measure that quantifies the dispersion or variability of a set of data compared to its mean and would thus provide us with information on how much the signal changed over time. A low standard deviation is desirable because it indicates that the signal is stable and predictable.

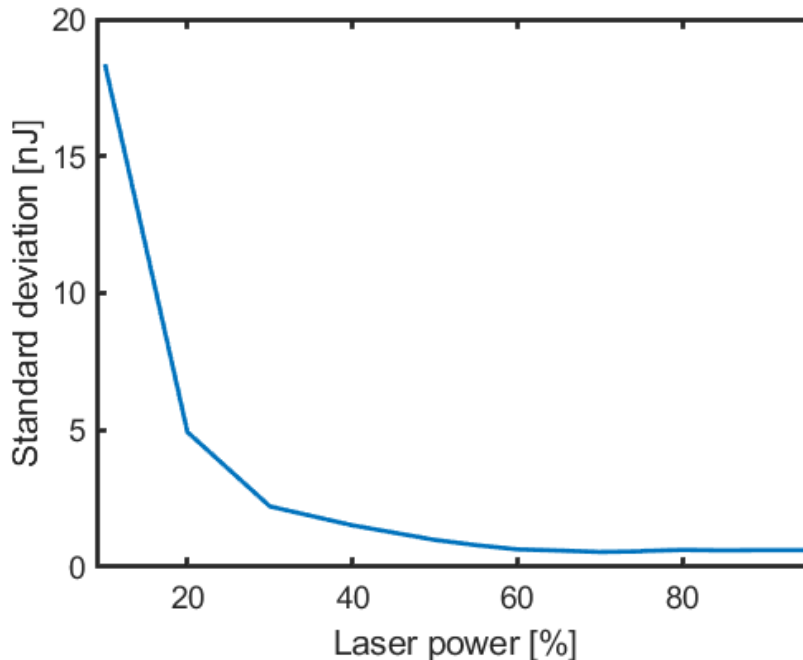
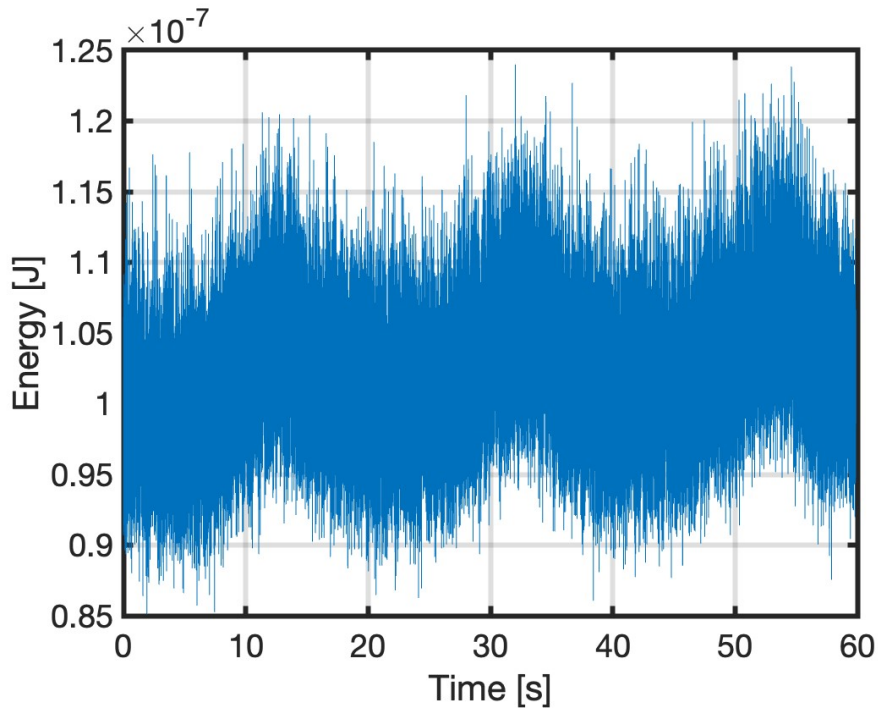


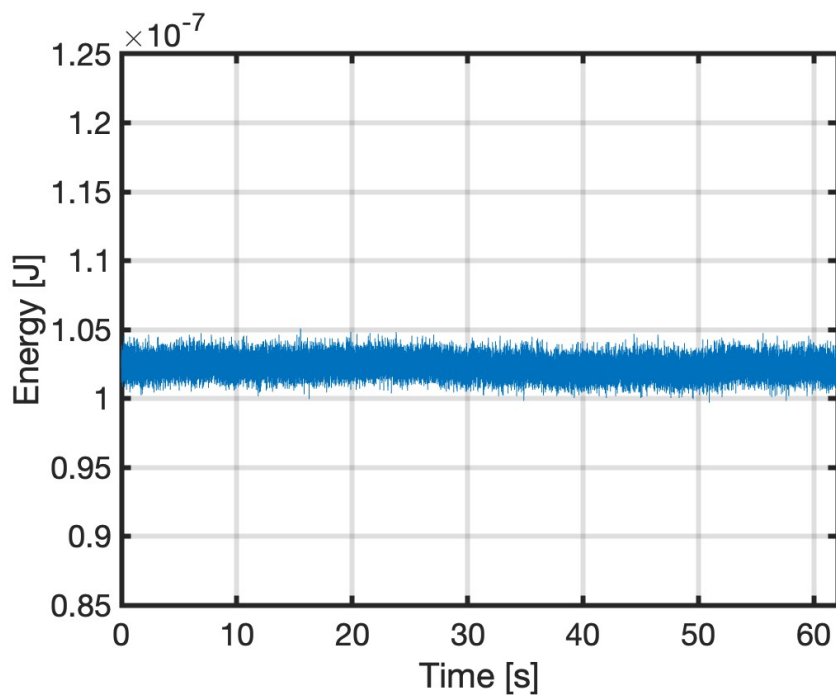
Figure 26 | *Distribution of the standard deviation at the various % of laser power.*

In agreement with what is shown in the graph above we noticed that the signal was very unstable when a low % was used, such as 20% for example (Fig. 27a), and instead began to be very stable

around 60% (Fig. 27b). From 60% to 95% the differences in stability are very minimal so we opted to continue the project using 60% power.



a.



b.

Figure 27 | Acquired data from measurements with the energy meter after the variable neutral density filter before and after a low-pass filter with a cutoff frequency of 100 Hz. (a) Graph of the values recorded with a power of 20% and central energy set at 1.025 nJ. (b) Graph of the values recorded with a power of 60% and central energy set at 1.025 nJ.

Returning to the problem encountered in the evaluation of the lateral resolution, however, having used a power of 50%, the signal loss would still be strange given that, as can be seen from Fig. 25, the beam at that power appears stable.

We then decided to try to perform the same measurement with 60% power after the optical fiber into which the beam was coupled. This time we increased the energy of the beam to around 200 nJ recording a period of around 60 s (Fig. 28).

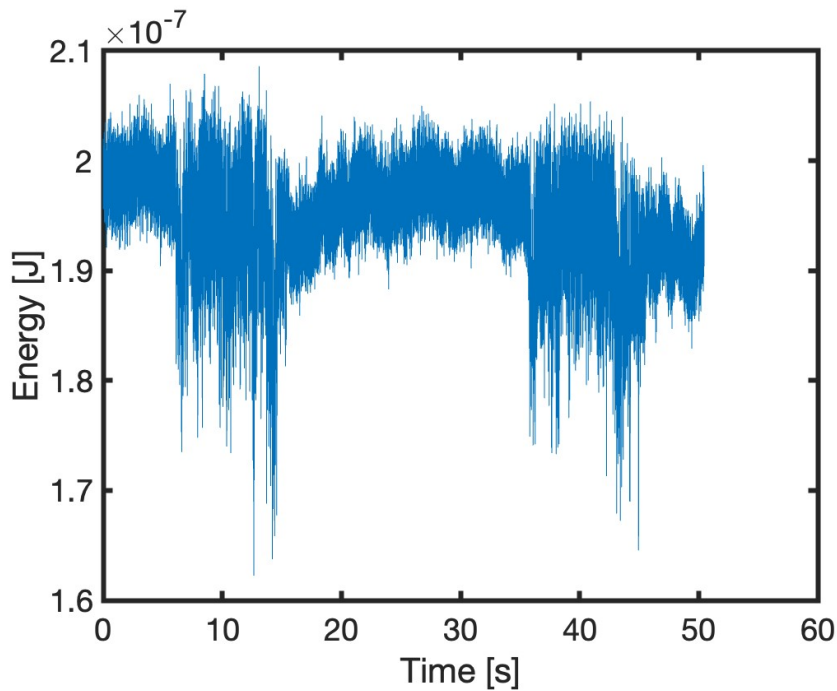


Figure 28 | *Acquired data from measurements with the energy meter after the optical fiber with a power of 60% and central energy set at 2 nJ.*

As we can see from the graph above, we have random oscillations of the laser energy, which are not random. We noticed that they occurred when a cooling fan located at the top of the excitation laser was activated.

This therefore caused vibrations of the laser box which led to a decrease in the coupling efficiency of the laser with the optical fiber. Even though they were minimal, they managed to shift the direction of the beam by those few um which were enough to have a decidedly lower output energy (we had a loss of about 20%).

These measurements led us to conclude that, given that the acquisition of an image with many samples and a high number of averages lasted a few minutes, the blurry lines that we previously noticed in the image for the lateral resolution (Fig. 21a) were due to the excitation laser cooling fan activation.

CHAPTER IV

5 DOPPLER EFFECT APPLICATION

At this point the device worked quite well, and each hitch had received a satisfactory explanation. The next and final step of our work was to try to detect the Doppler effect from the PA signal of moving microspheres.

The Doppler effect is a physical phenomenon that occurs when a wave source, such as sound, moves relative to an observer. When the source approaches the observer, the emitted waves are compressed, leading to an increase in the perceived frequency and a consequent rise in the tone of the sound. Conversely, if the source moves away, the waves lengthen, causing a decrease in perceived frequency and a lowering of the tone. This effect is commonly used in many fields, such as measuring the speed of objects, and provides valuable information on their direction of movement.

The device setup had to be slightly modified to continue with the next experiments (Fig. 29).

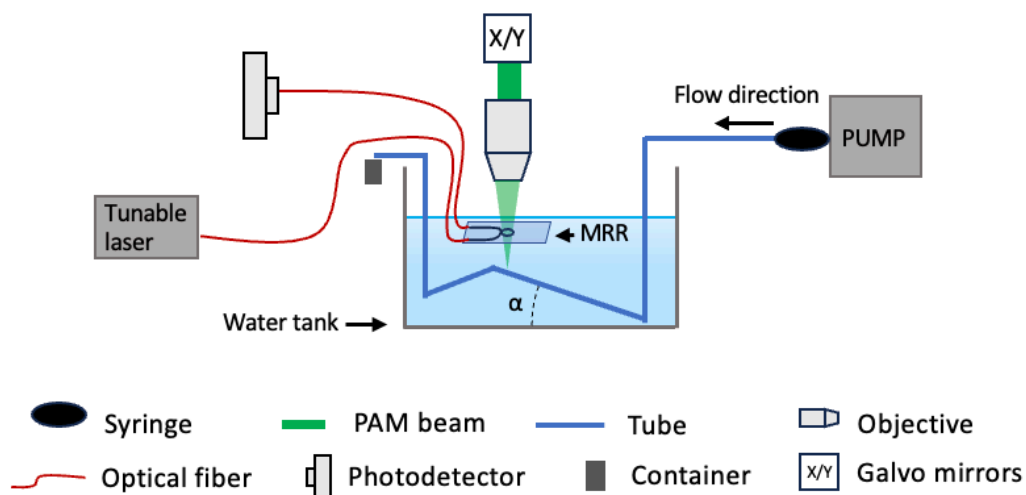


Figure 29 | *Schematic of the device adapted for Doppler effect measurements.*

As we can see from the figure above, we introduced a pump that allowed us to have a constant flow at a speed chosen by us inside a tube connected to the syringe placed on the pump. The tube also had to have a certain angle α with the MRR because otherwise we wouldn't be able to see any approach/departure effect of the source from the sensor.

We used the Harvard Apparatus' Pump 11 Pico Plus Elite which is a precision syringe pump designed for applications requiring extremely accurate and stable fluid flow control, a syringe with a diameter of 16 mm and a tube with a diameter of 1.5 mm (Fig. 30).

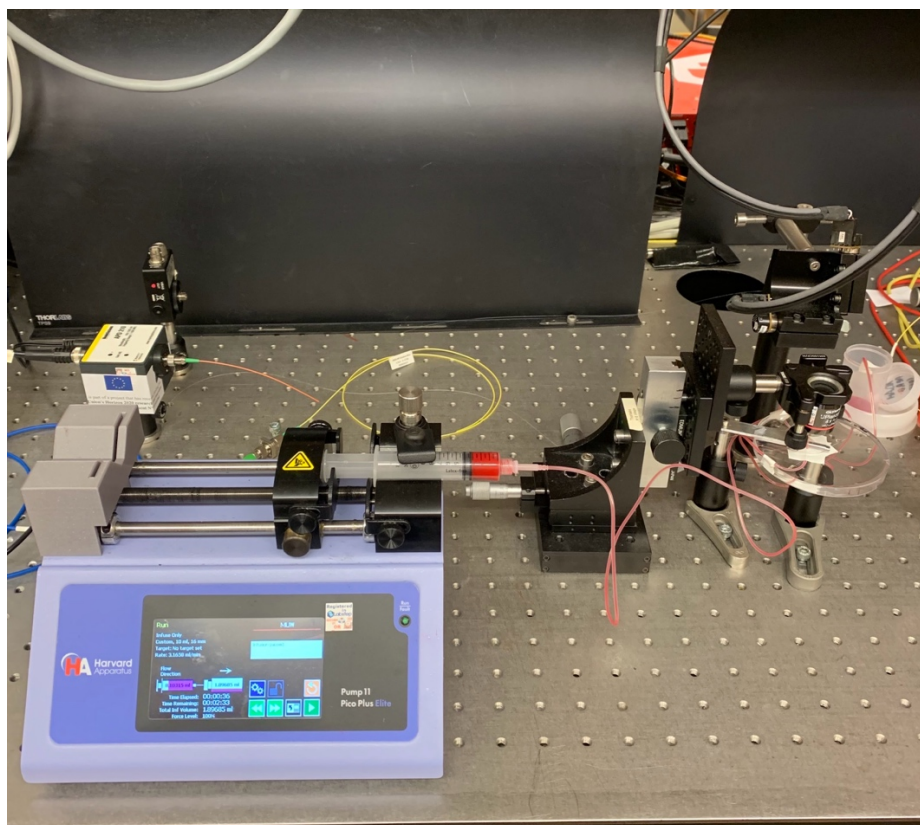


Figure 30 | Pump setup.

In accordance with the literature [9] we made a suspension containing 0.4×10^8 red dyed microspheres per milliliter (particle mean diameter: $6.0 \mu\text{m}$; 15714-5, Polysciences) using distilled water. We added sodium polytungstate (71913, Sigma- Aldrich) to avoid sedimentation and TWEEN 20 (P1379, Sigma-Aldrich) at 1% volume to prevent aggregation. We chose to prepare 10 mL of suspension, using 7.5 mL of dH_2O , 1.9 mL of microspheres, 0.75 g of sodium polytungstate and 0.1 mL of TWEEN 20. We also placed a container at the end of the tube to collect and reuse the fluid.

After we had prepared everything, we quickly encountered the first issue: the glass cover of the MRR (Fig. 6d) was too wide, preventing us from angling the tube beyond 20° . At steeper angles, the distance between the sensor and the microparticles would have been too great, making it impossible to acquire any signal. Even at this small angle, the distance was still too large for the sensor's limited sensitivity. Therefore, we decided to set α at 20° without testing other angles, despite knowing that larger angles could yield better results. The measurement of this angle was not precise, as the tube's inclination, constrained by the issue mentioned earlier, was only achievable using an iron piece to create a rise, and the tube was secured with tape.

The basic idea behind this experiment was to shoot two consecutive excitation laser pulses and acquire the two signals generated (Fig. 31), using a firing frequency of 10 kHz. These two signals were to be processed subsequently.

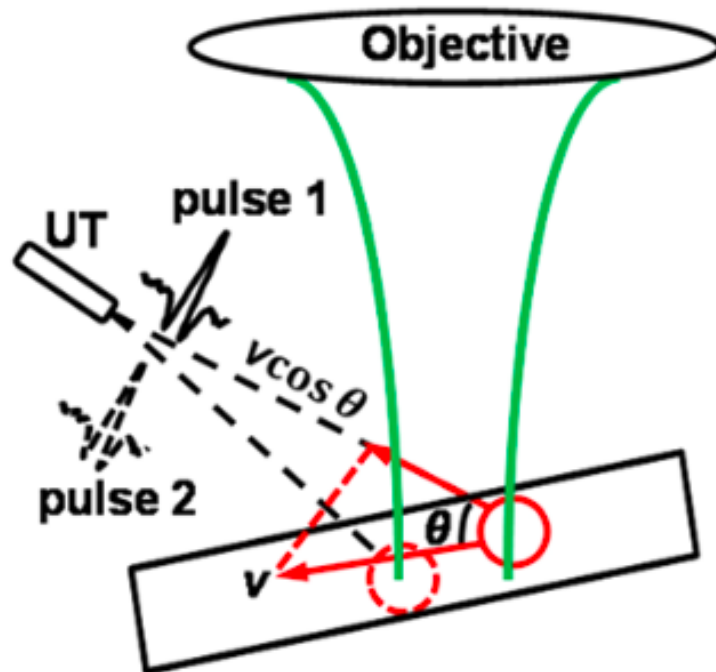
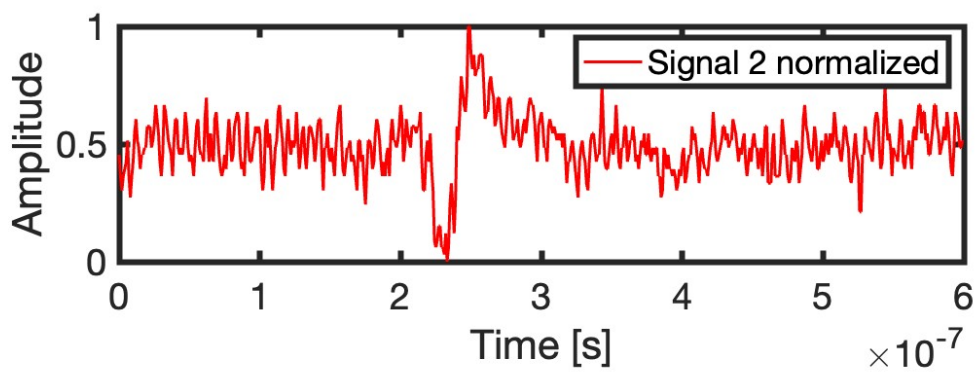
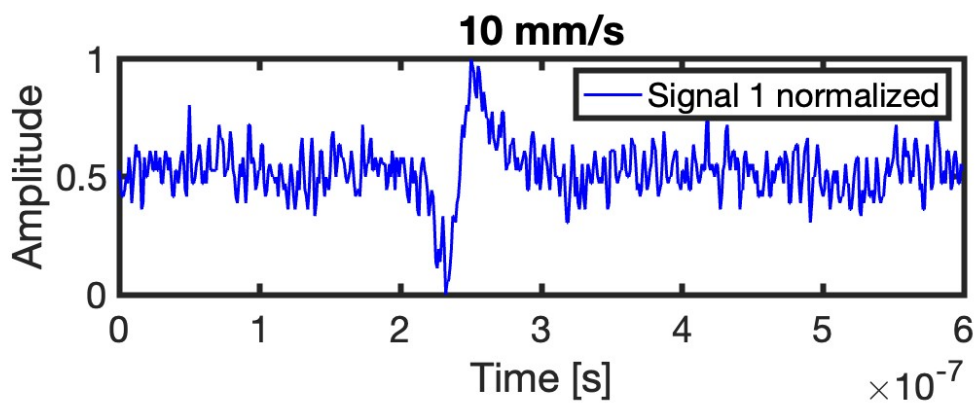
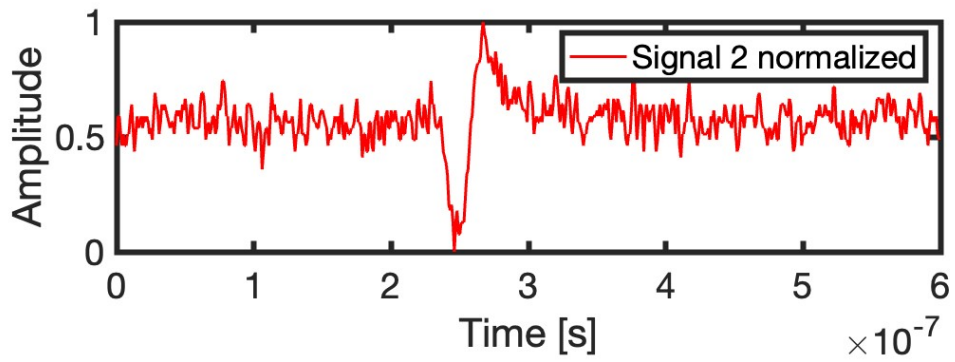
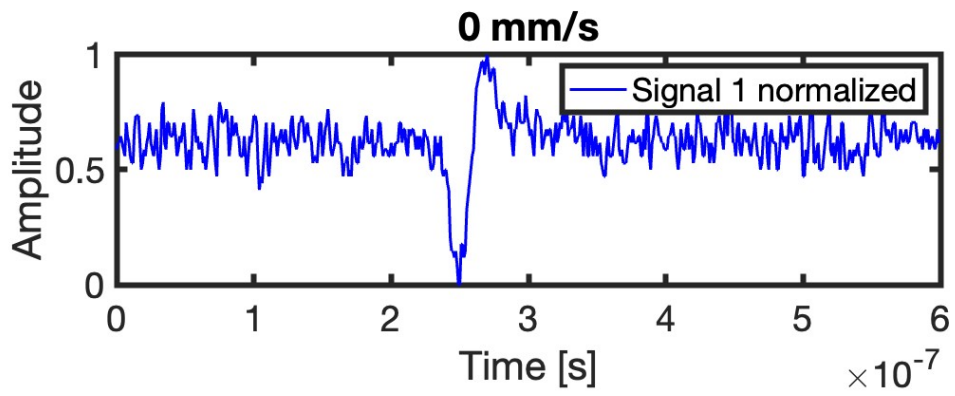


Figure 31 | *Principle of operation of the device for detecting Doppler effect [9].*

We started looking for the signal with the pump turned off and the liquid so not in motion to facilitate the arrangement of the objective and the tuning of the wavelength of the tunable laser. A second issue was soon identified: due to the size of the glass cover on the MRR, the distance between the sample and the sensor was too great (a few microns). As a result, we had to use a laser excitation power on the sample of $250 \mu\text{W}$ to achieve a signal of acceptable size and maximize the signal-to-noise ratio (SNR). However, this increased the risk of damaging the optical fiber to which the excitation laser was coupled.

We first acquired a signal with the liquid stationary to use as a baseline for comparison with subsequent signals, where we set the liquid speed in the tube to 10 mm/s and 20 mm/s as shown in the literature [9]. After multiple attempts, the best signal pairs for each analyzed speed are shown below (Fig. 32).



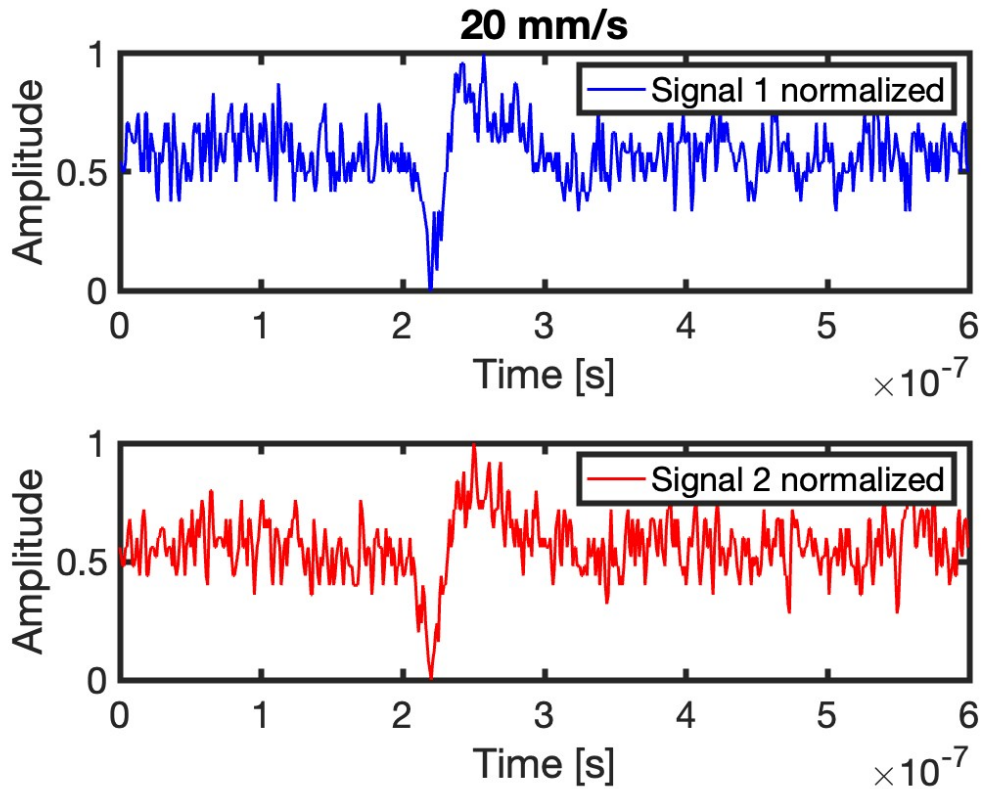
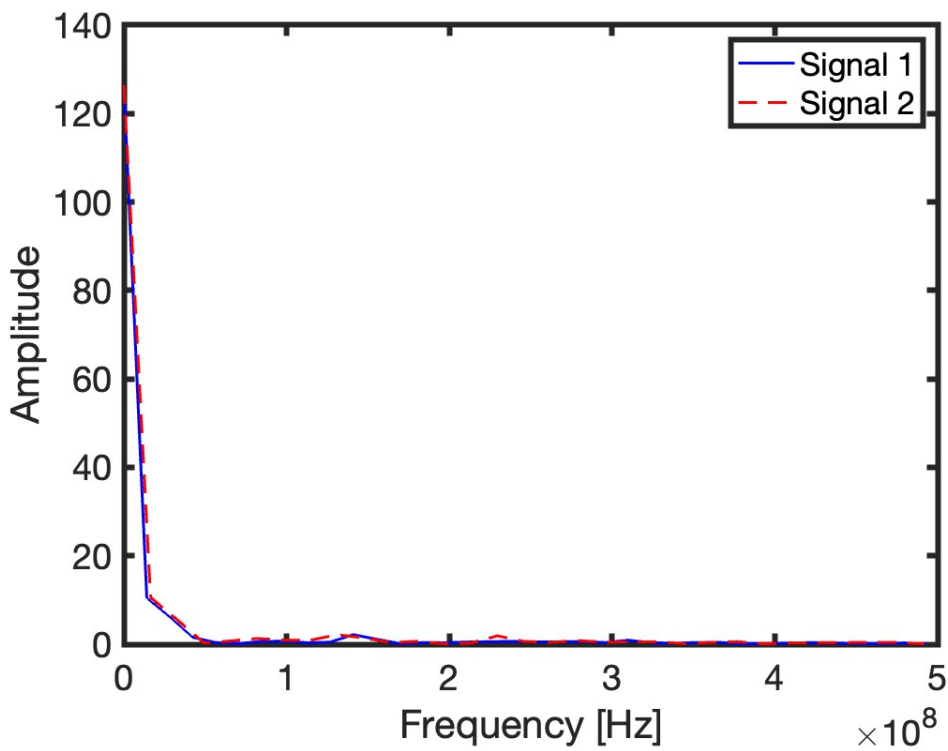
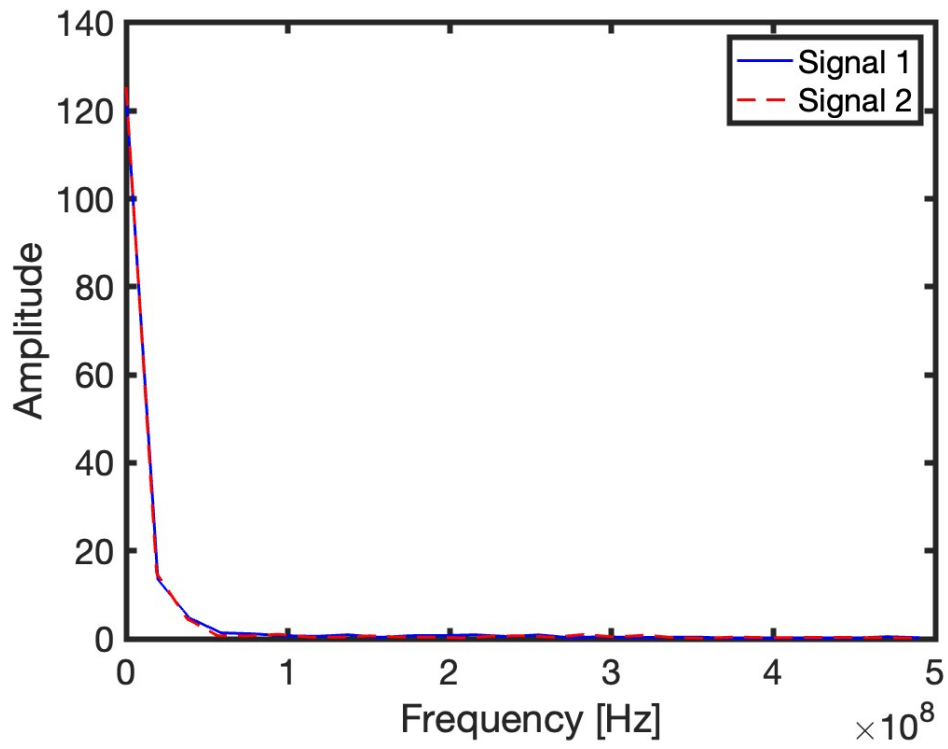


Figure 32 | Pairs of normalized signals for each speed: the first two correspond to signals with the liquid at rest, followed by signals at a liquid velocity of 10 mm/s, and in the end at 20 mm/s.

Once these signals were acquired, the first step was to check if the FFT of the second signal showed a shift towards higher frequencies compared to the FFT of the first signal. This shift was anticipated because we were analyzing an approaching source by positioning the beam on the tube's ascent rather than its descent. By comparing the FFT of the second signal to that of the first, we expected to observe this frequency shift (Fig. 33).



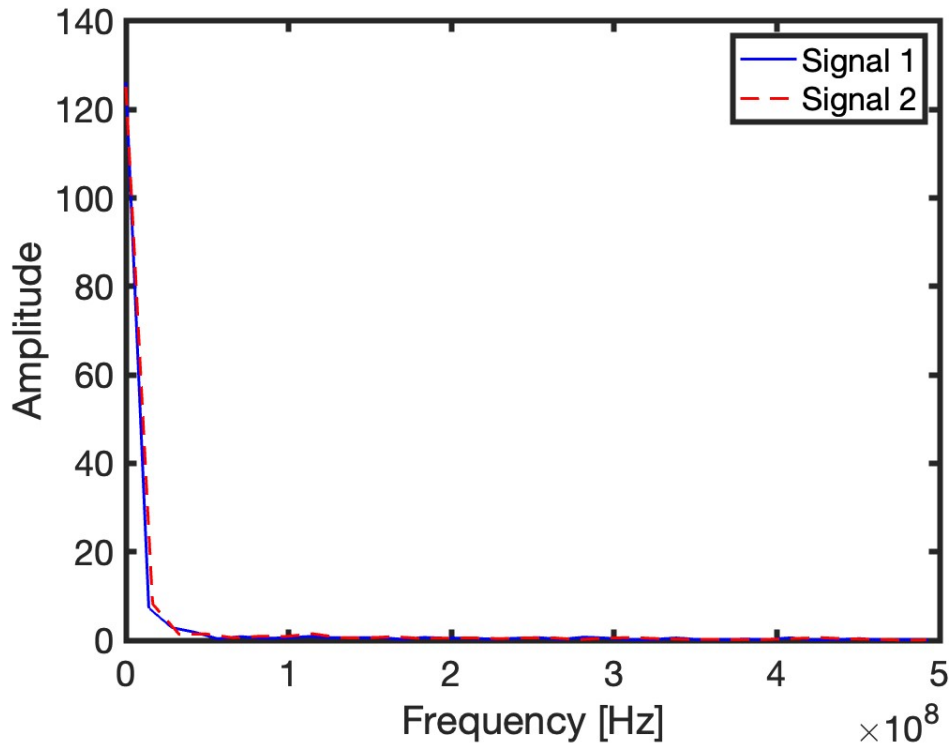
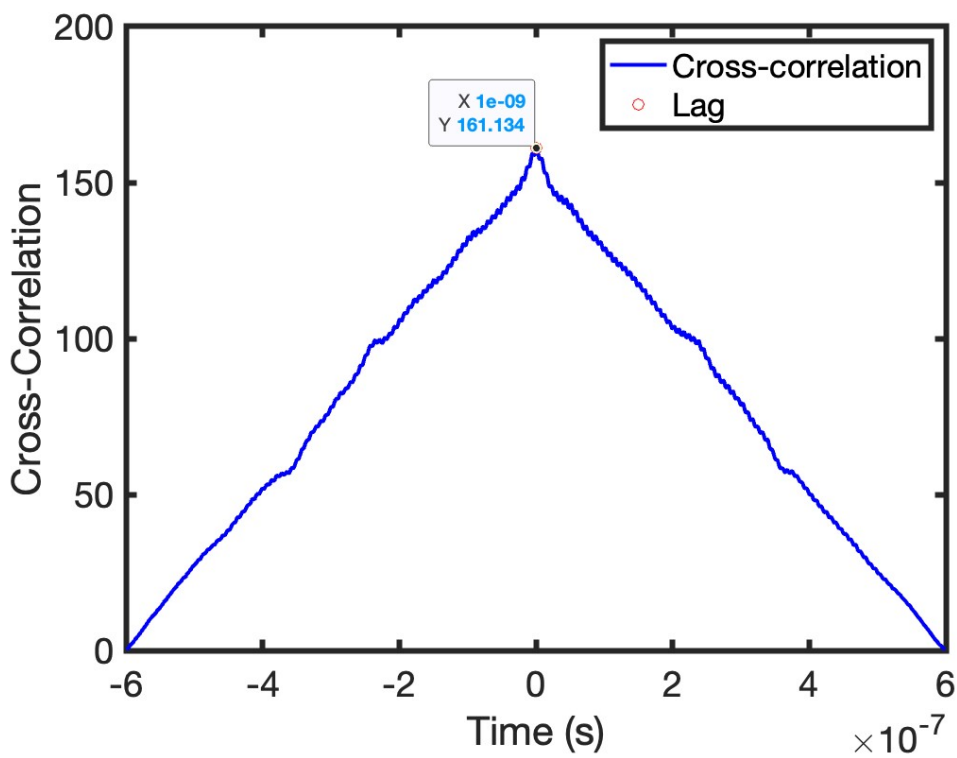
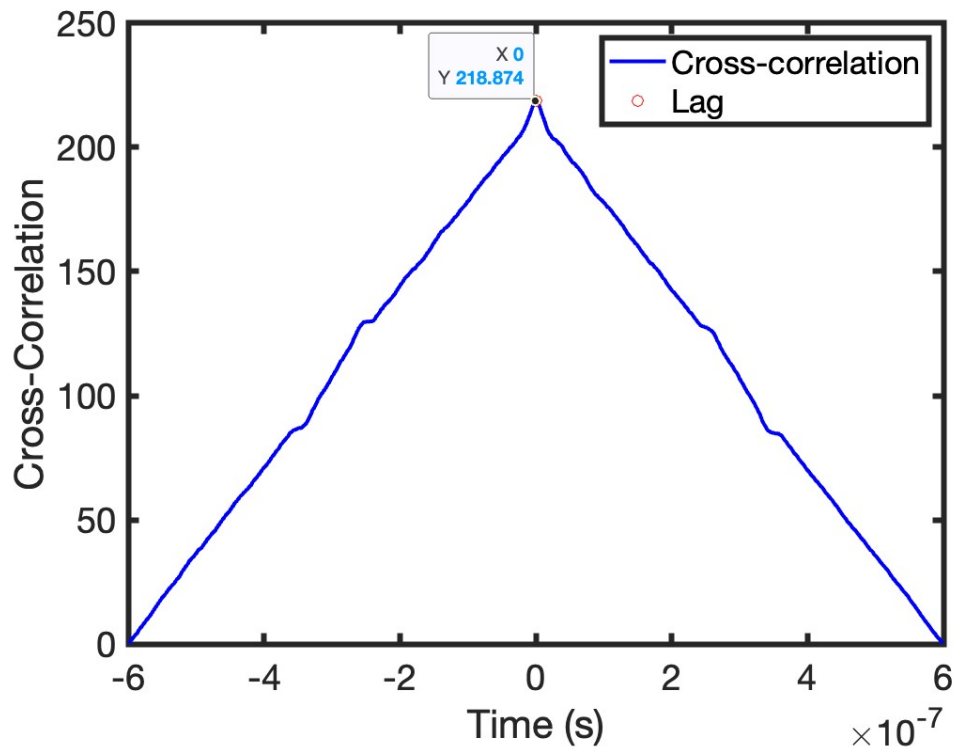


Figure 33 | *FFT compared between the two signals in the three analyzed cases, arranged in the same order as before.*

As shown in the graphs above, when the liquid was stationary, the FFTs of the two signals were nearly identical. However, when the fluid was set in motion, we observed a slight shift towards higher frequencies in the FFT of the second acquired signal. Unfortunately, however, this shift was indeed very small and possibly insignificant and cannot be definitively attributed to the Doppler effect.

We identified a third issue with the MRR: insufficient sensitivity. With greater sensitivity, the shift towards higher frequencies might have been more pronounced and attributable to the Doppler effect instead of potential noise.

At this point, as the last step, we tried to calculate the flow velocity using the formula $v = c \cdot t_s / (T \cdot |\cos(\alpha)|)$ [9], where c is the speed of sound in water, t_s is the time-of-flight (ToF) difference between two consecutive PA signals, and T is the time interval between the two laser pulses, that having a laser firing frequency of 10 kHz was 100 μ s. The time shift t_s was determined by performing temporal correlation between the two consecutive PA signals (Fig. 34). We employed cross-correlation because it is a method for determining the time delay, or lag, between two signals by evaluating their similarity as one signal is shifted relative to the other.



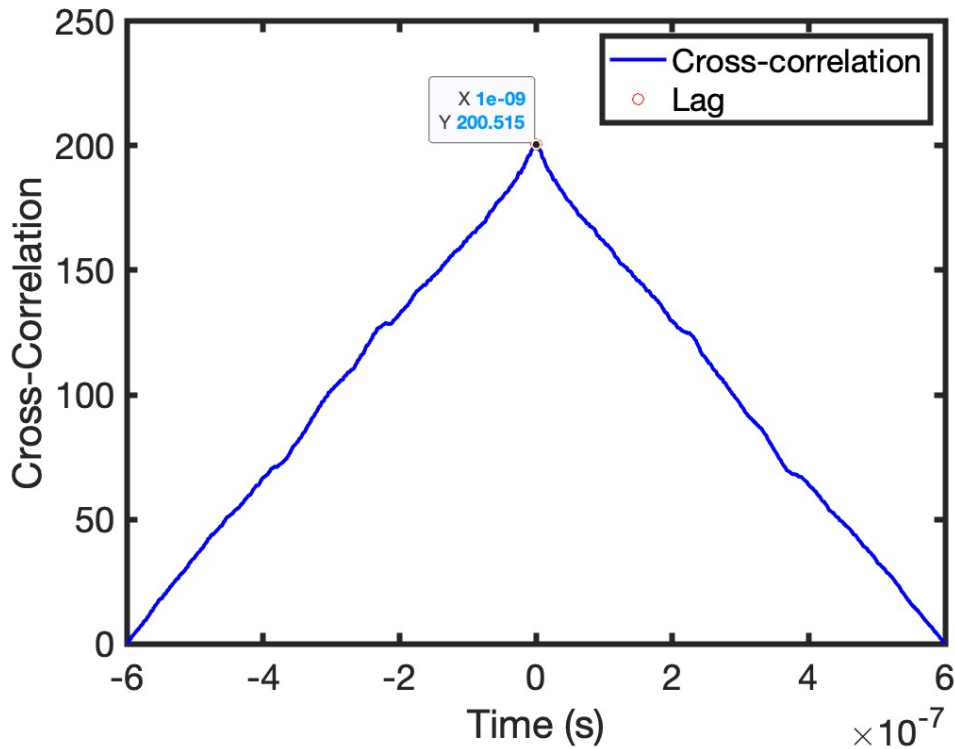


Figure 34 | *Cross-correlation between the two signals with the lag highlighted in seconds, arranged in the same order as before.*

As depicted in the figure, there is no delay between the two signals when the liquid is stationary. However, when the liquid is in motion, a delay of 1 ns is observed, which corresponds to t_s in the formula mentioned above.

It was easy to determine, however, through simple calculations, that the measured speed was the same in both instances when the liquid was in motion, as the lag between the two signals was identical, resulting in a speed of 16 mm/s, which is not too far from the set speed. When analyzing the formula, it became evident that the calculated delay would have to be significantly more accurate to distinguish the two cases with the moving liquid. We believe this issue arises, as previously mentioned, from the insufficient sensitivity of the sensor used.

In conclusion, we identified two primary issues that impeded this study on the Doppler effect: the size of the glass cover protecting the MRR and its low sensitivity. Both problems are related to the manufacturing process, and therefore, only limited improvements could be made within a short timeframe to enhance the results. However, future advancements in MRR production could provide a promising area for further investigation.

6 CONCLUSIONS AND FUTURE DEVELOPMENTS

During this project, we faced numerous challenges related to the characterization and optimization of micro-ring resonator (MRR) based devices and gained valuable information about their capabilities and limitations. Our analysis focused on three main aspects: device characterization, the stability of the excitation laser and the detection of the Doppler effect by moving microspheres.

During the characterization phase, we found a poor image quality with marked blurring of lines. This led us to consider the possible role of the instability of the excitation laser as a factor affecting the accuracy of measurements. We also observed a problem with the MRR waveguide buses, which blocked the laser pulse and were visible in large images. The parameters obtained at the end of this phase were a Q factor of 4.47×10^4 , a lateral resolution of $5.5 \mu\text{m}$, an axial resolution of $12 \mu\text{m}$ and a field of view of 0.8 mm .

Next, we focused on the analysis of the stability of the excitation laser, using an energy meter to monitor the beam behavior at different powers. We found that the beam was unstable at low power, but it became much more stable at 60% of maximum power, a value which we adopted for subsequent experiments. However, even after the laser was stabilized, we encountered another problem: the activation of the laser cooling fan caused vibrations, reducing the coupling efficiency with the optical fiber and causing a loss of energy of about 20%. This phenomenon explained the signal reduction observed during the characterization of the system.

In the end, we tried to detect the Doppler effect from microspheres in suspension. Although we were able to observe a slight shift towards higher frequencies in the signals acquired with the fluid moving towards the sensor, this shift was too small to be attributed with certainty to the Doppler effect. We identified two limiting factors: the size of the MRR protective glass, which prevented optimal angles for measurement, and the poor sensitivity of the sensor, which did not allow to clearly detect the Doppler phenomenon.

In conclusion, the work has revealed some limitations of the device, both in terms of manufacture and sensitivity. However, it has provided valuable insights into how to improve the system's design and stability for future applications. With further progress in the production of micro-ring resonators and an increase in sensitivity, the device could become a promising candidate for advanced imaging and detection applications based on optical and acoustic signals. Could be adapted and used in the EU's REAP project [10] to reveal drug tolerant persister (DTP) cells in breast cancer both in vitro and in vivo by contrast enhanced multimodal optical imaging.

7 BIBLIOGRAPHY

- [1] Jeon, S., Kim, J., Lee, D., Baik, J. W., & Kim, C. (2019). Review on practical photoacoustic microscopy. *Photoacoustics*, *15*, 100141. <https://doi.org/10.1016/j.pacs.2019.100141>.
- [2] Tutorial on photoacoustic microscopy and Computed tomography. (2008, February 1). IEEE Journals & Magazine | IEEE Xplore. <https://ieeexplore.ieee.org/abstract/document/4451136>.
- [3] Fu B, Cheng Y, Shang C, Li J, Wang G, Zhang C, Sun J, Ma J, Ji X, He B. Optical ultrasound sensors for photoacoustic imaging: a narrative review. *Quant Imaging Med Surg*. 2022 Feb;12(2):1608-1631. doi: 10.21037/qims-21-605. PMID: 35111652; PMCID: PMC8739120.
- [4] Ren, D.; Sun, Y.; Shi, J.; Chen, R. A Review of Transparent Sensors for Photoacoustic Imaging Applications. *Photonics* 2021, *8*, 324. <https://doi.org/10.3390/photonics8080324>.
- [5] Deng, Z., Li, C., Jing, L., et al. (2019). Deep learning photoacoustic imaging: A review. *Nature Communications*, *10*, 5120. <https://doi.org/10.1038/s41467-019-12178-6>.
- [6] Li, H., Dong, B., Zhang, Z., Zhang, H. F., & Sun, C. (2014). A transparent broadband ultrasonic detector based on an optical micro-ring resonator for photoacoustic microscopy. *Scientific Reports*, *4*(1). <https://doi.org/10.1038/srep04496>.
- [7] Ye, J., Chen, C., Pu, H., Wang, Z., Fan, Y., & Shi, L. (2019). Disposable ultrasound-sensing chronic cranial window by soft nanoimprinting lithography. *Nature Communications*, *10*, 4164. <https://doi.org/10.1038/s41467-019-12178-6>.
- [8] Xu, M., & Wang, L. V. (2006). Photoacoustic imaging in biomedicine. *Review of Scientific Instruments*, *77*(4), 041101. <https://pubs.aip.org/aip/rsi/article-abstract/77/4/041101/913562/Photoacoustic-imaging-in-biomedicine>.
- [9] Hu, S., Maslov, K., & Wang, L. V. (2013). Laser-scanning Doppler photoacoustic microscopy. *Applied Physics Letters*, *102*(20), 203501. <https://doi.org/10.1063/1.4807480>.
- [10] Liu, M., Deloria, A. J., Haindl, R., Li, Q., Szakacs, G., Csiszar, A., Schrittwieser, S., Muellner, P., Hainberger, R., Pelaz, B., Polo, E., Del Pino, P., Penttinen, A., Guina, M., Niemi, T., Meiburger, K., Molinari, F., Menhard, C., Heidelin, J., . . . Drexler, W. (2021). REAP: revealing drug tolerant persister cells in cancer using contrast enhanced optical coherence and photoacoustic tomography. *Journal of Physics Photonics*, *3*(2), 021001. <https://doi.org/10.1088/2515-7647/abf02f>.